STUDY OF FLOW REGIMES IN MULTIPLY-FRACTURED HORIZONTAL WELLS IN TIGHT GAS AND SHALE GAS RESERVOIR SYSTEMS

A Thesis

by

CRAIG MATTHEW FREEMAN

Submitted to the Office of Graduate Studies of
Texas A&M University
in partial fulfillment of the requirements for the degree of

MASTER OF SCIENCE

May 2010

Major Subject: Petroleum Engineering

Study of Flow Regimes in Multiply-Fractured Horizontal Wells in Tight Gas and Shale Gas Reservoir Systems

STUDY OF FLOW REGIMES IN MULTIPLY-FRACTURED HORIZONTAL WELLS IN TIGHT GAS AND SHALE GAS RESERVOIR SYSTEMS

A Thesis

by

CRAIG MATTHEW FREEMAN

Submitted to the Office of Graduate Studies of
Texas A&M University
in partial fulfillment of the requirements for the degree of

MASTER OF SCIENCE

Approved by:

Co-Chairs of Committee,	Thomas A. Blasingame
	George J. Moridis
Committee Members,	Peter P. Valko
	Lale Yurttas
Head of Department,	Stephen A. Holditch

May 2010

Major Subject: Petroleum Engineering

ABSTRACT

Study of Flow Regimes in Multiply-Fractured Horizontal Wells in Tight Gas and
Shale Gas Reservoir Systems. (May 2010)
Craig Matthew Freeman,
B.S., Texas A&M University
Co-Chairs of Advisory Committee, Dr. Thomas A. Blasingame
Dr. George J. Moridis

Various analytical, semi-analytical, and empirical models have been proposed to characterize rate and pressure behavior as a function of time in tight/shale gas systems featuring a horizontal well with multiple hydraulic fractures. Despite a small number of analytical models and published numerical studies there is currently little consensus regarding the large-scale flow behavior over time in such systems.

The purpose of this work is to construct a fit-for-purpose numerical simulator which will account for a variety of production features pertinent to these systems, and to use this model to study the effects of various parameters on flow behavior. Specific features examined in this work include hydraulically fractured horizontal wells, multiple porosity and permeability fields, desorption, and micro-scale flow effects. The theoretical basis of the model is described in Chapter I, along with a validation of the model.

We employ the numerical simulator to examine various tight gas and shale gas systems and to illustrate and define the various flow regimes which progressively occur over time. We visualize the flow regimes using both specialized plots of rate and pressure functions, as well as high-resolution maps of pressure distributions. The results of this study are described in Chapter II.

We use pressure maps to illustrate the initial linear flow into the hydraulic fractures in a tight gas system, transitioning to compound formation linear flow, and then into elliptical flow. We show that flow behavior is dominated by the fracture configuration due to the extremely low permeability of shale.

We also explore the possible effect of microscale flow effects on gas effective permeability and subsequent gas species fractionation. We examine the interaction of sorptive diffusion and Knudsen diffusion. We show that microscale porous media can result in a compositional shift in produced gas concentration without the presence of adsorbed gas. The development and implementation of the micro-flow model is documented in Chapter III.

This work expands our understanding of flow behavior in tight gas and shale gas systems, where such an understanding may ultimately be used to estimate reservoir properties and reserves in these types of reservoirs.

DEDICATION

This thesis is dedicated to my family and friends for their help and support.

What I cannot create, I do not understand.

— Richard Feynman

I do not think there is any thrill that can go through the human heart like that felt by the inventor as he sees some creation of the brain unfolding to success.

— Nikola Tesla

ACKNOWLEDGEMENTS

I want to express thanks to the following people:

Dr. Tom Blasingame for his mentoring and his standard of perfection.

Dr. George Moridis for sharing the tricks of the trade.

Dr. Peter Valko and Dr. Lale Yurttas for serving as members of my advisory committee.

TABLE OF CONTENTS

CHAPTER Page

LIST OF FIGURES

FIGURE Page

FIGURE Page

LIST OF TABLES

TABLE Page

CHAPTER I

INTRODUCTION

1.1 Statement of the Problem

Various analytical models have been proposed to characterize rate/pressure behavior as a function of time in tight/shale gas systems featuring a horizontal well with multiple hydraulic fractures Mattar *et al.* (2008). Despite a few analytical models as well as a small number of published numerical studies there is currently little consensus regarding the large-scale flow behavior over time in such systems, particularly regarding the dominant flow regimes and whether or not reservoir properties or volume can be estimated from well performance data. Tight gas and shale gas reservoirs are complex and generally poorly understood.

1.2 Objectives

Through modeling, we seek to represent the physical processes underlying these phenomena to demonstrate their effects on pressure and rate behavior in tight gas and shale gas systems, specifically those with complex fracture stimulation treatments. We hope to find a more rigorous method for understanding production characteristics, including estimation of reserves and evaluations of stimulation effectiveness.

1.3 Basis of Model Design

Once again, our primary objective is to characterize well performance in horizontal wells with multiple hydraulic fractures in tight gas/shale gas reservoir systems, incorporating all of the physics of these systems pertaining to transport and storage. To this end, we modified the TOUGH+ (TOUGH+ 2009) reservoir simulation code to incorporate those features.

The TOUGH family of simulation tools for multiphase flow and transport processes in permeable media was developed at and is maintained by researchers in the Earth Sciences division of Lawrence Berkeley National Laboratory. The specific branch of code which served as the starting point for this work is TOUGH+, which is the TOUGH code rewritten in Fortran 1995 in order to take advantage of modern amenities afforded by the development of that language. The current stewards of the TOUGH+ (TOUGH+ 2009) code base are Dr. George Moridis and Dr. Matt Reagan.

Fortran is a programming language particularly suited for numeric computation and scientific applications. The language was specifically developed for fast and efficient mathematical computations. The mathematical operators in Fortran (such as addition, multiplication, etc.) are intrinsic precompiled binaries

_____

This thesis follows the style and format of the *SPE Journal*.

rather than invoked classes, making Fortran faster than other popular languages such as C++ (Chapman 2008).

Fortran is thus particularly well-suited to reservoir simulation — as an example, the popular reservoir simulator Eclipse (Eclipse 2008) is coded in Fortran.

The fundamentals of petroleum engineering reservoir simulation are well-established in the literature. In lieu of a detailed discourse on reservoir simulation basics, we will here describe the specific implementations included in our model.

As received, the TOUGH+ (TOUGH+ 2009) code was capable of isothermal black-oil flow. The code used in this work has been extended to include the features relevant to flow in shale gas/tight gas reservoir systems. Two-phase flow of aqueous and gas phases is modeled. Both phases are treated compositionally, where the properties of methane, ethane, water, carbon dioxide, etc. are treated independently, as opposed to the simplified "black oil" model.

Discretization of the time and space solution domains is performed using dynamic time-step adjustment and extremely fine spatial gridding in three dimensions. The equations describing mass flux and mass accumulation are solved simultaneously for all grid blocks via the Jacobian matrix. We are now able to discuss the manner in which the terms of these equations are computed in a given internal iteration.

The density of the gas phase is computed by the Peng-Robinson (Peng and Robinson 1976) equation of state as a function of the pressure, composition, and temperature value of the grid element. The viscosity of the gas phase is computed by the Chung *et al.* (1988) model. The saturated dissolution concentration of the gas species in the aqueous phase is computed by use of Henry's parameter. Multiple options are included for the modeling of two-phase flow dependent properties. Primarily, the van Genuchten (1980) model is used for capillary pressure determination, and the Corey (1957) model is used for relative permeability determination.

In the case of two-phase flow and single-phase gas flow, the primary variables of simulation are pressure and mole fractions of the individual gas species in the gaseous phase. Where only one gas component is present (typically a pure methane simulation) then the only primary variable is pressure. In cases where thermal considerations are considered to be important, there is the potential for temperature to be included as the final primary variable. However, the thermal consideration is neglected in this work, as the gas flowrates are typically very slow, and Joule-Thompson cooling can be assumed to be minimal.

The most substantial alterations to the model concerned the area of appropriate simulation grid creation for modeling of horizontal wells with multiple transverse hydraulic fractures, as well as various assumptions of complex-fractured volumetric grids. It was determined that extremely fine discretization of the grids near the tips, junctions, and interfaces of reservoir features (such as near the wellbore, near the fracture

face, and at the tips of the fractures and the wellbore) would be required in order to adequately model the early-time well performance where pressure gradients are extremely sharp in this region. This rationale ultimately led to the use of grids having up to one million grid cells for a volumetric region no larger than several meters on a side.

A second area of substantial improvement concerned the dynamic permeability alteration as a function of pressure and composition via the microflow model. The mathematical development and validation of this method is described in Chapter III. The purpose of this method was to adequately capture the transport effects of micro-scale porous media.

1.4 Validation

There exist no current exact solutions for the complex problems being studied in this work. However, there are ample solutions to simpler problems which may be used to verify the various parts of the model individually. In this section, we verify the functionality of our reservoir model by comparison to an analytical solution, a commercial reservoir simulation package (Eclipse 2008) and a field case of a Haynesville shale gas well.

1.4.1 Case 1: Analytic Solution Match

This case considers flow of a slightly compressible fluid into a vertical well at a constant production rate. The model of this work (TAMSIM) is compared against the analytic solution for pressure in an infinite-acting radial system having slightly compressible fluid,

$$p_D(t_D, r_D) = \frac{1}{2} E_1\left[\frac{r_D^2}{4t_D}\right] \quad \text{.....(1.2)}$$

where

$$t_D = 2.637\times10^{-4}\frac{k}{\phi\mu c_t r_w^2}t \quad \text{.....(1.3)}$$

$$p_D = 7.081\times10^{-3}\frac{kh}{qB\mu}(p_i - p_r) \quad \text{.....(1.4)}$$

and

$$r_D = \frac{r}{r_w} \quad \text{.....(1.5)}$$

The reservoir parameters used in this model match are contained in **Table 1.1**. **Fig. 1.1** depicts the parameters in **Table 1.1** employed in both the TAMSIM model and the analytic solution expressed in Eq. 1.2.

We observe a close match between the two cases. The most significant deviation occurs near the wellbore. Due to the manner in which the analytic solution treats the nonlinearity of the fluid compressibility, it is likely the case that TAMSIM is more physically correct than the analytic solution.

Table 1.1 — Model parameters for the analytic solution match, slightly compressible fluid, radial reservoir.

Model Parameters

k	=	100 md
ϕ	=	0.2
h	=	10 m
r_e	=	10,000 m
p_i	=	300 bar
T_i	=	30 C
q	=	1 kg/s
B	=	1
c_t	=	2×10^{-9} 1/Pa

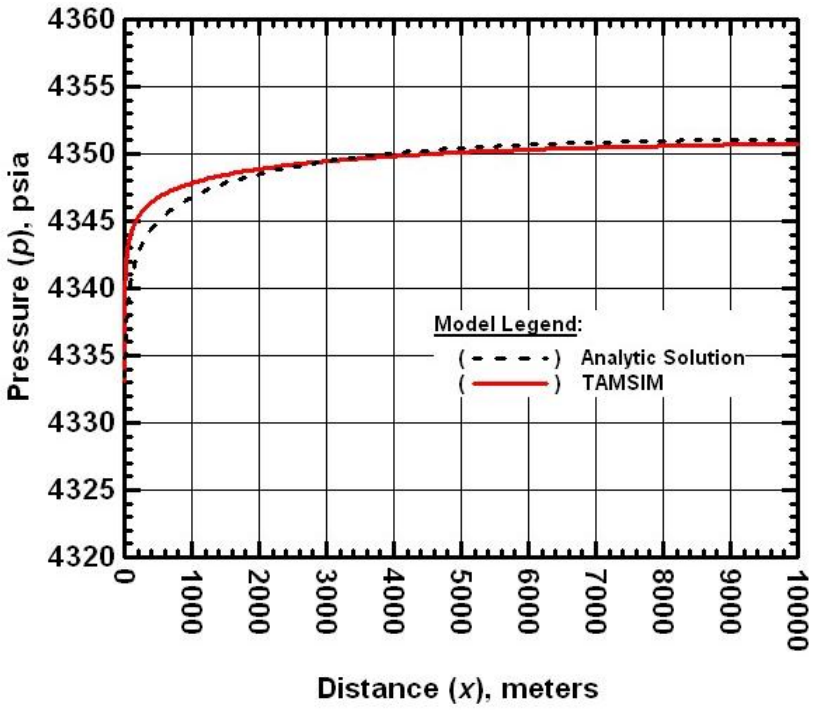

Figure 1.1 — Numerical model of this work (TAMSIM) matched against infinite-acting radial analytic solution described in Eq. 1.2 with properties contained in **Table 1.1**.

1.4.2 Case 2: ECLIPSE Solution Match

This case considers flow of a gas into a vertical well at a constant bottomhole flowing pressure. The simulation parameters are contained in **Table 1.2**. The TAMSIM case is compared against the reservoir simulator ECLIPSE given the same input parameters. This well is effectively infinite-acting.

Fig. 1.2 depicts the parameters in **Table 1.2** employed in both the TAMSIM model and the ECLIPSE reservoir simulator.

Table 1.2 — Model parameters for the ECLIPSE model match, gas properties, radial reservoir.

Model Parameters

k	=	0.01 md
ϕ	=	0.1
h	=	30 ft
r_e	=	50,000 ft
r_w	=	3.6 in
p_i	=	5000 psia
q	=	50 mscf/d
c_f	=	1×10^{-9} 1/psi

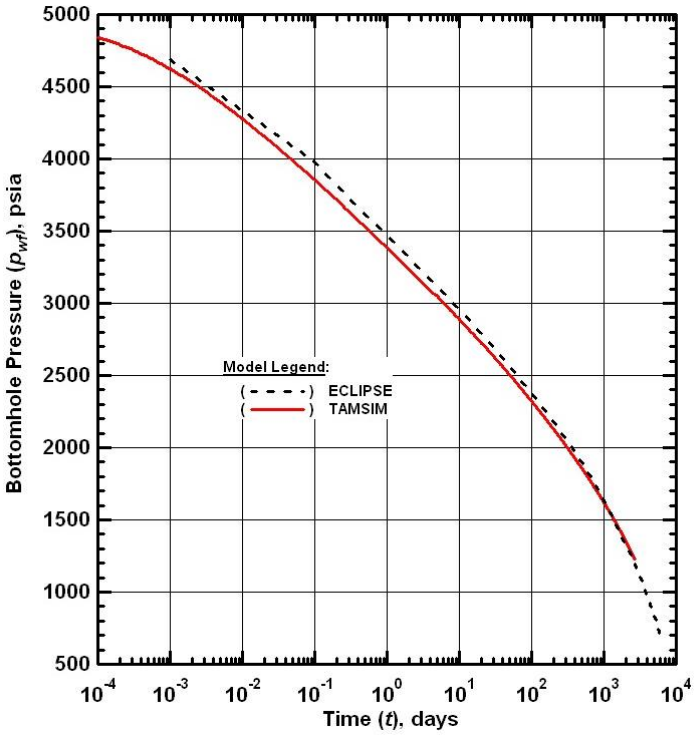

Figure 1.2 — Numerical model of this work (TAMSIM) compared against commercial reservoir simulator ECLIPSE using properties contained in **Table 1.2**.

We observe an excellent match for the entire problem domain. It should be noted that ECLIPSE uses a user-specified lookup table for computing fluid properties as a function of pressure. In order to achieve this match, Eclipse (Eclipse 2008) was provided with a lookup table generated by the Peng-Robinson (Peng and Robinson 1976) equation of state internal to TAMSIM.

1.4.3 Case 3: Haynesville Shale Gas Well Match

This case considers a real horizontal well with ten transverse fractures in the Haynesville shale. A model match was performed on the available pressure/rate data using the TOPAZ module of the Ecrin software package by Kappa (Ecrin 2009). The model parameters of best fit were used as inputs for TAMSIM to achieve this match. The strategy of matching was to simulate one repetitive element and to multiply that rate by a factor of 80 to match the production from the entire horizontal well system. The effective fracture conductivity of the repetitive element was adjusted slightly to improve this match. The model match parameters are given in **Table 1.3**.

Table 1.3 — Model match parameters for Haynesville shale gas well acquired using TOPAZ software package, used as inputs for TAMSIM model. Results plotted in **Fig. 1.5.**

Model Parameters

k	=	0.0028 md
x_f	=	225 ft
C_{fD}	=	1.05×10^{5}
d_f	=	114.9 ft
ϕ	=	0.03
h	=	100 ft
L_w	=	4150 ft
r_w	=	3.6 in
p_i	=	11005 psia
p_{wf}	=	3000 psia
c_f	=	3×10^{-6} 1/psi

The match parameters obtained in **Table 1.3** are from a TOPAZ model fit and are used to generate the simulated data shown in **Fig. 1.3** (Ecrin 2009).

The gas flowrate match appears to be excellent. It would be an exaggeration to claim that TAMSIM correctly history-matched this well without including flowing water and variable bottomhole pressure production. However, TAMSIM did very accurately replicate the TOPAZ model match result, which led to the replication of the rate behavior (Ecrin 2009).

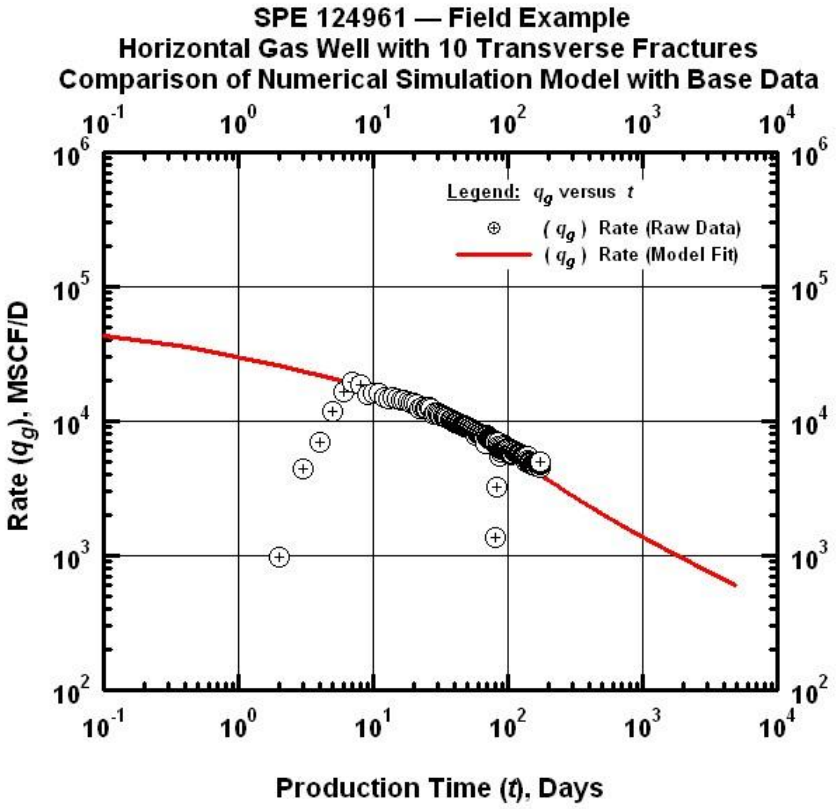

Figure 1.3 — Numerical model of this work used to match a model fit for a Haynesville shale gas well. Note that while the rate match is excellent, the auxiliary matches are inferior. This is because the model of this work operates at constant bottomhole pressure.

1.5 Summary and Conclusions

We have successfully developed and validated the single-phase gas functionality of the numerical simulator for horizontal wells with transverse hydraulic fractures. In the course of this work, we employ this model to study the flow regimes present in this configuration. Specifically, we have examined the interactions between reservoir parameters (permeability, sorptivity, porosity, and pressure), completion parameters (fracture spacing, fracture conductivity) and the flow regime effects in order to characterize those effects.

In this work we characterize the influence of various reservoir and completion parameters on performance of multiply-fractured horizontal wells in ultra-low permeability reservoir systems.

1. Contrary to intuition, the effect of desorption can be accounted for by a time-scaling constant. The presence of desorption appears to shift fracture interference forward in time.

2. We have developed a formulation for numerical computation of microscale flow phenomena in porous media and implemented and verified its veracity.

3. While a dual porosity model may appear to fit field performance data, such a model will not correctly represent the effects of fracture interference. Fracture interference is an inescapably transient effect which *appears* to mimic boundary-dominated flow but, this is not the correct interpretation of this behavior.

None of these three features/observations is a true reservoir boundary. Due to the relatively small volumes of investigation of these well systems, it is unlikely that reservoir compartmentalization is the true cause of "boundary-dominated flow" effects as interpreted from rate data.

The features of higher permeability, higher fracture conductivity, higher induced fracture complexity, and more highly fractured reservoir will all lead to a higher initial rate and initial dimensionless rate, yet late time dimensionless rates will merge with lower permeability/conductivity/complexity cases sometime during the compound linear flow period. The effect of desorption, on the other hand, is more apparent at late time than early time, tending to prolong all flow periods and extend production.

1.6 Recommendations for Future Work

This work will be continued as follows:

1. Inertial (Forchheimer) flow in propped fractures is known to impact production in high-rate wells. This should be modeled and its effect studied.
2. The presence of water should be included in a rigorous study of the flow regime behavior.
3. The mechanism of formation damage caused by fracturing fluid is a likely culprit in the relative success or failure of stimulation treatments. Modeling of the behavior of this damage zone and the flowback of fracturing fluids should be performed for a complete picture of near-wellbore transport.

CHAPTER II

LITERATURE REVIEW

Our approach has been to determine the proper theoretical foundation for creating a tight gas/shale gas simulator via an intensive literature search, and to implement the relevant concepts into the purpose-built numerical simulator TAMSIM, which is based on the TOUGH+ (TOUGH+ 2009) numerical simulators. The literature search focused on the physics and simulation of coalbed methane, tight gas, and shale gas reservoirs. Specific storage and transport mechanisms were investigated, including flow in fractured porous media; microscale flow; surface sorption; two-phase non-linear flow models; and geomechanics of shale.

2.1 Planar Hydraulic Fracture Model

In order to hydraulically fracture a well, a fluid is pumped at a high rate and pressure into the wellbore, usually followed by some volume of proppant (Mattar *et al.* 2008). The high pressure of the fluid will induce a high stress deep underground, and the rock will tend to fracture at the point of perforation. A typical proppant is well-sorted sand or synthetic material, which will move into the crack created by the injected fluid. After the pumping of fracturing fluid ceases, natural tectonic stress will force the fracture closed; however, the proppant pack in the fracture is designed to prevent total closure, providing a high-conductivity flow path from the well deep into the formation.

This view of hydraulic fracturing treats the fracture as an essentially planar crack in the rock which propagates away from the wellbore in a direction perpendicular to the least principal tectonic stress (Mattar *et al.* 2008). In the example of a horizontal well drilled in the direction of least principal stress, at sufficient depth that the greatest principal stress is vertical, the crack will orient itself perpendicularly to the wellbore. A well of this type may be fractured multiple times along its length in an attempt to expose more surface area to a greater volume of the reservoir. This is called a horizontal well with multiple transverse fractures, or a multiply-fractured horizontal well.

2.2 Flow Concept of van Kruysdijk and Dullaert

Various attempts have been made in the literature to characterize the progressive flow regimes in reservoirs with horizontal wells with multiple fractures. The flow concept of Dullaert and van Kruysdijk (1989) postulate that the flow into horizontal wells with multiple fractures can be divided into relatively discrete periods. First, fluid flows straight into the fractures in a linear manner, called "formation linear flow" (**Fig. 2.1**). As the pressure transient propagates away from the fractures, these linear impulses interfere. There follows a period of transition where the region between the fractures is depleted and the outer edge of the pressure transient gradually shifts its orientation such that the bulk flow is now linear

toward the collection of fractures. Thus the formation linear period culminates in a second linear period called "compound formation linear" flow. According to these authors, pseudo-radial flow toward the well-fracture system does not manifest until an order of magnitude later in time. The shape of this transient is shown to be elliptical.

The existence of these flow regimes, in any case involving interference between fractures, introduces severe complexity into any attempt to model or predict well performance (Mattar *et al.* 2008). The early signature of fracture interference in pressure and rate data is indistinguishable from the signature of no-flow reservoir boundaries. Consequently, fracture interference, or, the beginnings of compound-linear flow, is commonly misinterpreted as boundary-dominated flow. As we will show in this work, the time until fracture interference is not trivial to predict, and depends on many factors including sorptive storage, fracture spacing and complexity, fracture treatment effectiveness, ultra-low permeability, and pressure dependencies on permeability.

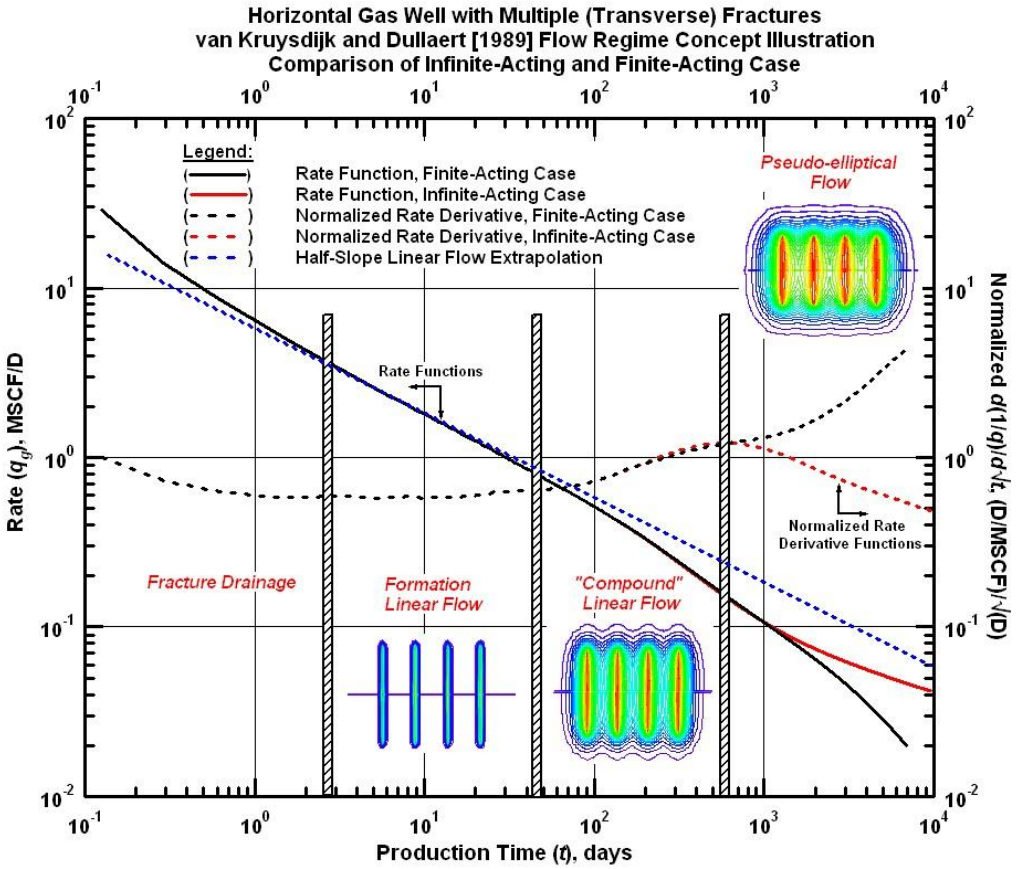

Figure 2.1 — Demonstration of Van Kruysdijk and Dullaert (1989) flow regime progression on rate and normalized rate derivative behavior.

The presence of multiple distinct "unconventional" characteristics in shale gas/tight gas reservoirs render a unique diagnosis of reservoir and completion parameters from rate/pressure data very difficult or impossible. Whatever properties may have been diagnosed in simple well completion models are confounded by the progressing flow regimes caused by horizontal wells with multiple hydraulic fractures. The approach of this work is to systematically vary these important reservoir and completion parameters within typical engineering ranges to characterize the impact of each parameter on well performance, with a particular attention paid to the interaction of rate/time behavior with the flow regime progression.

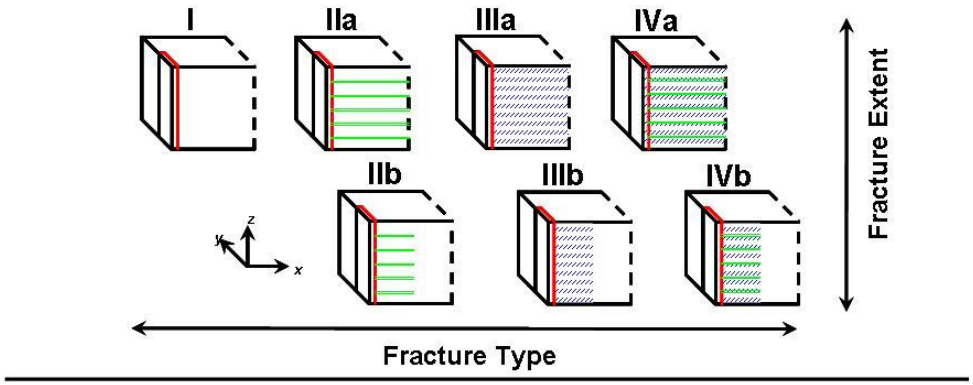

I. Planar fracture, transverse fracture only.
IIa. Planar fracture, stimulated thin lateral layers.
IIb. Planar fracture, with stimulated thin lateral layers, partial extent.
IIIa. Planar fracture, with naturally fractured shale.
IIIb. Planar fracture, with naturally fractured shale, partial extent.
IVa. Planar fracture, stimulated layers and fractured shale.
IVb. Planar fracture, stimulated layers and fractured shale, partial extent.

Figure 2.2 — Possible *in situ* fracture configurations. The vertical axis ("fracture extent") denotes how far into the reservoir the secondary fracturing has reached. The horizontal axis ("fracture type") differentiates between single planar fractures (I), fractures intersecting horizontal high-conductivity layers (II), complex-fractured zones (III), and a combination of all features (IV).

Many models exist for inflow into single vertical fractures. Raghavan *et al.* (1997) provide a mathematical description of inflow into the late-time compound-linear flow regime. Medeiros, Ozkan and Kazemi (2006) introduced a semi-analytical solution capable of modeling the range of flow regimes surrounding a multiply-fractured horizontal well system. Medeiros, Ozkan and Kazemi (2007) extended this idea beyond the assumption of planar hydraulic fractures to include dual permeability zones near the fracture faces. The basis of these dual permeability zones is to represent a complex-fractured region surrounding the primary hydraulic fracture. The existence of such a complex fracture network has been

corroborated by real-time microseismic observation of fracture treatments and has come to be referred to as the so-called "stimulated reservoir volume" (SRV) concept. We suggest a "continuum" of possible complex fracture layouts in the near-wellbore reservoir, ranging from the planar fracture case to a dual porosity fractured reservoir case, illustrated in **Fig. 2.2**.

These semi-analytical models are robust, but do not account for desorption or a change of permeability as a function of reservoir pressure over time. Desorption can be a significant source of produced gas, and no analytic models exist which include desorption. Permeability change in shales as a function of reservoir pressure may occur either due to matrix shrinkage or Knudsen flow effects.

Current models for rate-decline prediction and reserves estimation/production forecast from early time data in ultra-tight reservoir systems fail to account for fracture interference, and consequently yield extremely optimistic predictions (Currie, Ilk, and Blasingame 2010). A primary goal of this paper is to address this confusion.

2.3. Petrophysics and Geology

Tight gas and shale gas reservoirs present numerous challenges to modeling and understanding. These reservoirs typically require fracture stimulation, which creates complex systems of fractures and thus complex flow profiles. Additionally, according to Hill and Nelson (2000), between 20 and 85 percent of total storage in shales may be in the form of adsorbed gas. The majority of this gas may never be produced due to the steepness of the sorption isotherm at lower pressures. Production from desorption follows a nonlinear response to pressure and results in an unintuitive pressure profile behavior. Closed or open natural fracture networks in ultra-tight reservoirs introduce further complexity through connection with the induced hydraulic fractures.

Gas desorption from kerogenic media has been studied extensively in coalbed methane reservoirs, where adsorption can be the primary mode of gas storage. Many analytic and semi-analytic models have been developed from the study of gas desorption from coalbed methane reservoirs, including transient responses and multicomponent interactions (Clarkson and Bustin 1999). However, the sorptive and transport properties of shale are not necessarily analogous to coal (Schettler and Parmely 1991). Complex coal-based desorption models provide no additional insight over the commonly used empirical models for single-component surface sorption, the Langmuir (1916) isotherm (given by Eq. 2.1):

$$\theta = \frac{pV_L}{p + p_L} \quad \text{.....(2.1)}$$

The desorption isotherms as proposed by Langmuir are typified by the V_L term which expresses the total storage at infinite pressure and the pressure at which half of this volume is stored (p_L). Further, the Langmuir model assumes instantaneous equilibrium of the sorptive surface and the storage in the pore

space. From a modeling perspective, this means there is no transient lag between pressure drop and desorption response. Due to the very low permeability of shales, flow through the kerogenic media is extremely slow, so instantaneous equilibrium is a good assumption (Gao *et al*. 1994).

The presence and state of natural fractures varies on a reservoir-by-reservoir (or even well-by-well) basis. In some cases, it is believed that fracture stimulation effectively re-opens an existing, yet dormant or sealed natural fracture network through alteration of near-wellbore stresses (Medeiros, Ozkan, and Kazemi 2007). In other cases, a true planar vertical fracture is believed to be formed (Mattar *et al*. 2008).

Many models have been proposed to model pressure- and stress-dependent properties of porous media. There are a number of complex models which relate permeability, total stress, effective stress, and various rock properties such as by pore compressibility, Young's modulus, and other parameters, as described by Davies and Davies (2001) and Reyes and Osisanya (2002). A typical application of the theory of stress-dependent petrophysical properties is the prediction of *in situ* porosity and permeability from core analysis results.

Stress regimes may change in the near-fracture region during depletion. Whether or not dynamic interactions between local stress and pressure are important to production characteristics may be the subject of future work. In this work we make the assumption that the stress regimes do not significantly change after the initial fracture treatment has taken place. Where total stress is assumed to be constant, we are able to model changes in porosity and permeability purely as functions of a deviation from initial pressure. The assumption that *in situ* stress is constant and independent from reservoir pressure obviates the need for a fully coupled geomechanical model. We therefore assume a relatively straightforward model for pressure-dependent porosity described by McKee, Bumb and Koenig (1988),

$$\phi = \phi_o \exp[-c_p(p_i - p)] \quad (2.2)$$

and likewise, a simple relation for pressure-dependent permeability:

$$k = k_o \exp[-c_p(p_i - p)] \quad (2.3)$$

The values for c_p (*i.e*., the pore compressibility), is treated as a constant value in this work, although models exist which treat c_p as a function of pressure.

Water Saturation Dependent Properties

The presence of water in shale reservoirs introduces several issues; including capillary pressure effects, relative permeability effects, and phase change. So-called "clay swelling" may be important, and can be viewed as a special case of capillary pressure with different governing equations.

Ward and Morrow (1987) demonstrate the suitability of the Corey model as modified by Sampath and Keighin (1982) in tight sands (see Eq.2.4 below). Due to a lack of published data regarding relative permeability models for shales, we assume that the mineralological and petrophysical similarities between

shale and tight gas are sufficient that the tight gas relative permeability model can also be used for shale gas for our purposes in this work.

$$k_{rw} = \left[\frac{S_w - S_{wi}}{1 - S_{wi}}\right]^4 \left[\frac{k_w}{k_\infty}\right] \quad \text{.....(2.4)}$$

In Eq. 8,

$$k_w = k_\infty^{1.32} \quad \text{.....(2.5)}$$

Likewise, capillary pressure models for shale are unavailable. Additionally, the theoretical distinction between physical adsorption of water molecules and capillary absorption of water is unclear in porous media with extreme small scale pores found in tight gas and shale gas reservoirs. In other words, there is no functional difference between adsorption and capillary wetting in nanoporous media.

2.4 Forchheimer Flow

Forchheimer (1901) initially proposed a model to compensate for the nonlinear deviation from Darcy's law in high velocity flow. This model relates the pressure gradient to a quadratic function of flow velocity. Typically, flow tests must be performed on to calculate the Forchheimer β-parameter (Forchheimer 1901) representing the nonlinearity, but several models have been proposed to predict the Forchheimer β-parameter without first performing variable pressure tests on the formation of interest (Li and Engle 2001). Such a prediction is of particular interest where reservoir simulation is concerned. Due to the complex geometries of tight gas and shale gas wells created by stimulation treatments, it may be impossible to uniquely assess a β-parameter through testing. This is because the propped fractures, the secondary fractures, and the matrix may each have separate effective β-parameter.

$$-\nabla p = \frac{\mu}{k} v + \beta \rho v^2 \quad \text{.....(2.6)}$$

Models for prediction of the Forchheimer β-parameter are specific to single-phase flow versus two-phase flow, or consolidated versus unconsolidated porous media. In this work we are particularly interested in models for two-phase flow. The presence of water in the porous media significantly impacts the effective tortuosity, porosity, and permeability to the gas phase, all of which are correlated with the β-parameter. A relation determined by Kutasov (1993) (Eq. 2.7), based on experiment results, computes the β-parameter as a function of effective permeability to gas as well as water saturation, making it ideal for simulation purposes:

$$\beta = \frac{1432.6}{k_g^{0.5}[\phi(1 - S_w)]^{1.5}} \quad \text{.....(2.7)}$$

The β-parameter is given in 1/cm, k_g (effective permeability to gas) is in Darcy, and S_w [water saturation] is in fraction. Frederick and Graves (1994) also develop two empirical correlations for the β-parameter when

two-phase flow exists. These two forms (Eq. 2.8 and Eq. 2.9) are almost identical in character but different in form and computational simplicity. These correlations are given as:

$$\beta = \frac{2.11\times10^{10}}{k_g^{1.55}[\phi(1-S_w)]} \quad \text{.....(2.8)}$$

and

$$\beta = \frac{1}{[\phi(1-S_w)]^2}\exp[45-\sqrt{407+81\times\ln(k_g/(\phi(1-S_w)))}] \quad \text{.....(2.9)}$$

The β-parameter is given in 1/ft, k_g [effective permeability to gas] is in md, and S_w [water saturation] is in fraction.

For purposes of comparison, the β-parameters computed in Eq. 2.8 and Eq. 2.9, are relatively consistent; however, in comparison to the trend in Eq. 2.7, they vary by many orders of magnitude at lower intrinsic permeabilities. Flow through low-permeability rock will tend to have a low velocity, and is therefore unlikely to significantly exhibit inertial flow, so deviations in the models at low permeability may be unimportant.

Many models include a dependence on tortuosity; however, tortuosity is itself a function of porosity and water saturation (Li and Engler 2001), and is not independently known. To avoid confusing the physics we avoid the models which rely on tortuosity as an input parameter.

The proppant grains in a propped fracture are unconsolidated, so we are interested primarily in models for unconsolidated porous media. Cooke (1973) has correlated β-parameter coefficients to various proppant types by the relation in Eq. 4:

$$\beta = bk^{-a} \quad \text{.....(2.10)}$$

where b and a are empirical constants for the proppant type. In Cooke's (1973) work, the unit of the β-parameter is given in atm-sec^2/g. **Table 2.1** contains the proppant parameters from Cooke (1973).

Table 2.1 — Cooke *et al.* (1973) parameters for determination of Forchheimer β-coefficient for various proppants.

Sand Size (mm)	a (dimensionless)	b (atm-sec^2/g-md)
8-12	1.24	3.32
10-20	1.34	2.63
20-40	1.54	2.65
40-60	1.60	1.10

Since we have assumed that the β-parameter can be computed from state properties, we can implement this computed β-parameter into our numerical implementation. Darcy's law modified with the Forchheimer velocity-dependent term is given in Eq. 2.7

2.5 Thermal Effects

The primary driver of temperature change in a tight gas or shale gas reservoir would be the Joule-Thompson cooling inside the fractures due to gas rapid expansion. Nonisothermal conditions will also result in more correct pressure gradients due to thermodynamically correct gas expansion.

2.6 Molecular Flow Effects

Klinkenberg (1941) first observe that apparent permeability to gas will be a function of pressure in reservoirs with extremely low permeability to liquid. Florence *et al.* (2007) propose a theoretically derived model for predicting the apparent permeability as a function of the dimensionless Knudsen number of the gas flow, which depends on the mean pore throat radius and the gas species. The Florence micro flow equation expresses the apparent permeability as:

$$k_a = k_\infty [1+\alpha(Kn)Kn]\left[1+\frac{4Kn}{1+Kn}\right] \quad \text{.....(2.11)}$$

The function α is a rarefaction coefficient parameter, which is a dimensionless adjustment parameter of the form

$$\alpha(Kn) = \alpha_0 \frac{2}{\pi}\tan^{-1}[c_1 Kn^{c_2}] \quad \text{.....(2.12)}$$

Where c_1 is a constant valued at 4.0, c_2 is a constant valued at 0.4, and α_0 is a constant valued at $64/(15\pi)$. If the species-dependent Knudsen number is used, then the microflow formula, Eq. 11, will vary the apparent or effective permeability experienced by each individual gas species, due to the fact that each gas species in the mixture will have a different mean free path (as computed by Eq. 11) and thus a different Knudsen number. In this work, we extend the Florence *et al.* (2007) model to characterize multicomponent flow. The development and implementation of this method is given in Chapter IV.

CHAPTER III

NUMERICAL STUDY OF TRANSPORT AND FLOW REGIME EFFECTS

This chapter presents a study of the effects of various transport and storage parameters on flow well performance in a numerical model possessing simulation parameters and grids designed to represent tight gas/shale gas reservoir and completion systems. These effects include desorption via the Langmuir isotherm model, the behavior of which is depicted in **Fig. 3.1**.

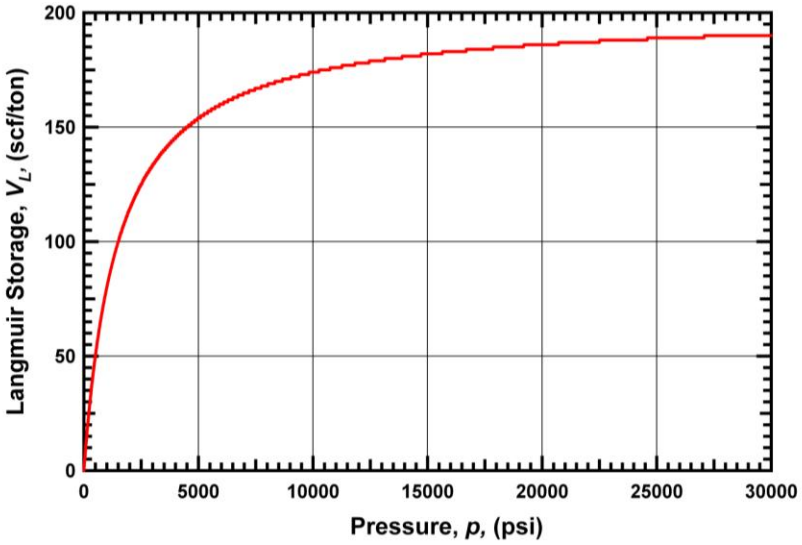

Figure 3.1 — Langmuir (1916) isotherm storage behavior as a function of pressure.

The goal of this work specifically is to characterize the interaction of parameters such as desorption with the van Kruysdijk and Dullaert (1989) flow regimes, the development and behavior of which are depicted in **Fig. 1.2**.

3.1 Description of Numerical Model Parameters

Several distinct gridding schemes were applied in this work. In the first set of simulation models, a fully three-dimensional, extremely finely discretized grid is used to accurately model the near-fracture region at very early times. The layout of this model and the manner in which these repeating well-system elements connect is illustrated in **Fig. 3.2**. Several grids of the same general design were created by varying the effective fracture spacing, d_f. For example, in the base case, the distance between the fracture and the no-flow barrier is 5 m (16.40 ft) corresponding to an d_f of 10 m (32.81 ft), and in the sensitivity cases, d_f

values of 5 m (16.40 ft) and effective d_f is 20 m (65.62 ft) are used. It is worth mentioning that in all cases, gravity is neglected due to the reasonably thin reservoir intervals concerned.

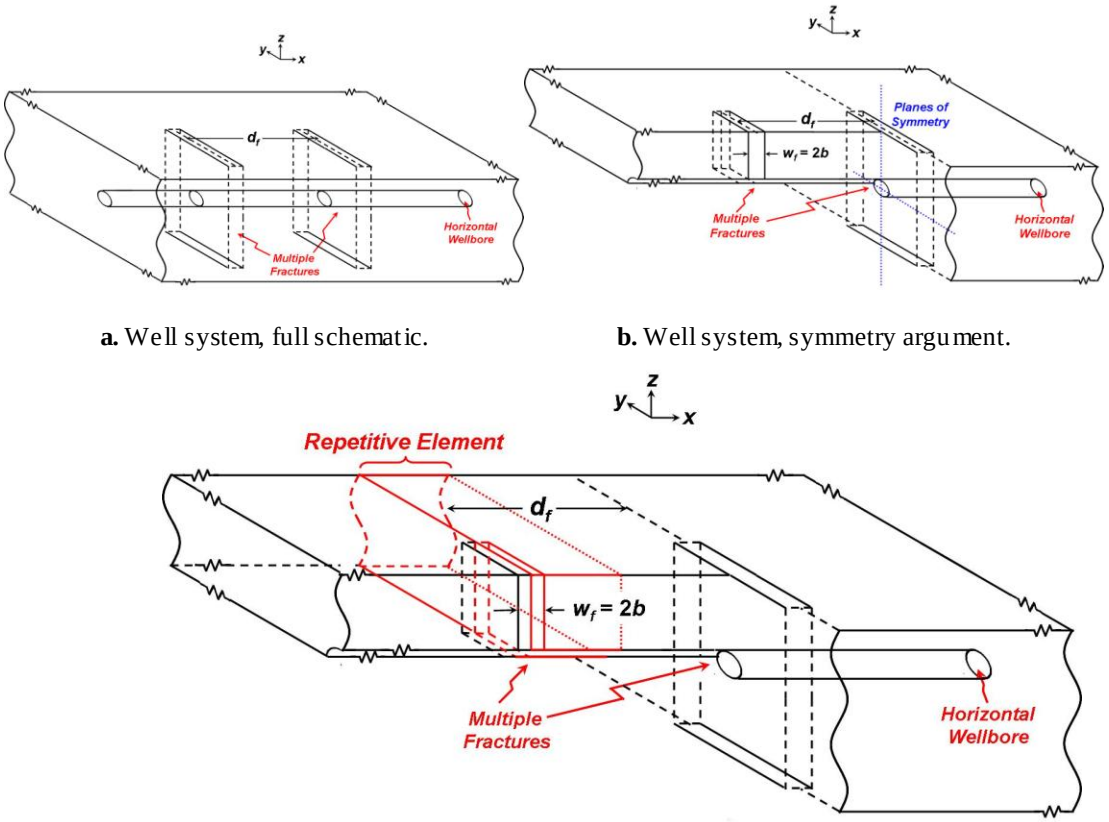

a. Well system, full schematic.

b. Well system, symmetry argument.

c. Well system, repetitive element represented.

Figure 3.2 — Schematic diagram of horizontal well/transverse fracture system in a rectangular reservoir (note that the "repetitive element" concept permits placement of evenly-spaced transverse (vertical) fractures).

The third set examines the effects of laterally continuous thin high permeability layers connected to the primary fracture, with and without microfractures in the shale.

The fourth set employs a fully transient highly fractured gridding scheme, utilizing a dual-porosity assumption. The purpose of this grid type is to approximate the "stimulated reservoir volume" (SRV) concept, that there are no true highly conductive planar fractures, instead there is a fractured region surrounding the well.

The fifth set represents both the features of the third and fourth sets, possessing both thin conductive horizontal layers and dual-porosity shale matrix.

The sixth and final grid scheme utilizes less finely discretized gridding and qualitatively demonstrates the large-scale late-time flow behavior of the system. We perform sensitivity analyses on these systems varying Langmuir volume and fracture width.

We treat the fracture as possessing a fixed dimensionless conductivity as proposed by Cinco-Ley, Samaniego, and Domingues (1978) in order to compare the conductivity with values obtained using other models. Consequently, we do not examine Forchheimer (1901) (inertial) flow, because this would conflict with the finite-conductivity fracture implementation. In this work, we use a range of fracture permeabilities corresponding to a wide range of dimensionless fracture conductivities, defined by Eq. 3.1:

$$C_{fD} = \frac{k_f w}{k_m x_f} \tag{3.1}$$

For example, a fracture with width of 0.1mm, possessing a dimensionless conductivity of 1.05, will possess a k_f equal to 10.6 md where the matrix permeability is 1.0×10^{-4} md. The fracture permeabilities (and consequently the fracture conductivities) used in the simulation cases are computed in **Table 3.1** below. The fracture permeabilities (and consequently the fracture conductivities) used in the simulation cases are shown in **Table 3.1** below.

Table 3.1 — Fracture permeabilities and equivalent dimensionless conductivities used in the simulation runs.

Fracture Permeability (md)	Reservoir Permeability (md)	Fracture Conductivity[31] (dimensionless)
10,555	1.0×10^{-4}	1.05×10^{4}
10.6	1.0×10^{-4}	1.05
0.0106	1.0×10^{-4}	1.05×10^{-4}
10,555	1.0×10^{-5}	1.05×10^{5}
10.6	1.0×10^{-5}	10.5
0.0106	1.0×10^{-5}	1.05×10^{-3}
10,555	1.0×10^{-3}	1.05×10^{3}
10.6	1.0×10^{-3}	0.105
0.0106	1.0×10^{-3}	1.05×10^{-5}

The Langmuir (1916) isotherm curve models desorption as a function of pressure. The Langmuir parameters are tuned to provide storage in a similar range found in known shale reservoirs. The Langmuir volume parameter (V_L in Eq. 1.1) is varied as shown in **Table 3.2** while the Langmuir pressure parameter

(p_L in Eq. 1.1) is held at initial reservoir pressure for all cases. The real properties of pure methane are computed as a function of pressure at isothermal conditions using the Peng-Robinson equation of state. Water flow is not modeled, as its interaction with the shale is poorly understood and would merely add a confounding influence to the results. Additionally, this would only hinder analytical comparison. The other pertinent simulation case parameters for Set A are presented in **Table 3.2**.

Table 3.2 — Description of the simulation runs and sensitivity analyses varying fracture conductivity.

Case	Fracture Spacing (m)	Permeability (nd)	C_{fD}	Langmuir Volume (scf/ton)
A1	10	10	1.05×10^{4}	0
A2	10	10	1.05×10^{4}	200
A3	10	10	1.05	0
A4	10	10	1.05	200
A5	10	10	1.05×10^{-4}	0
A6	10	10	1.05×10^{-4}	200

Table 3.3 — Description of the simulation runs and sensitivity analyses using highly refined gridding scheme.

Case	Fracture Spacing (ft)	Permeability (nd)	Perforations Per Fracture	Drawdown (psi)	Langmuir Volume (scf/ton)
B1	32.8	100	3	1000	100
B2	32.8	100	1	1000	100
B3	32.8	100	5	1000	100
B4	32.8	10	1	1000	100
B5	32.8	1000	1	1000	100
B6	32.8	100	1	1000	0
B7	32.8	100	1	1000	200
B8	16.4	100	1	1000	100
B9	65.6	100	1	1000	100
B10	32.8	100	1	1400	100
B11	32.8	100	1	4500	100
B12	32.8	100	1	1000	2000

We note that for all the cases in Set A, a matrix permeability of 10 nd was assumed. In all the cases in Set B, described in **Table 3.3**, a matrix permeability of 100 nd is assumed, except for the sensitivity cases where 10 nd and 1000 nd are shown. The full gridding scheme also uses 100 nd permeability.

3.2 Results and Analysis

We will first discuss the base case results. Then the effects of various completion parameters will be analyzed. Next we will discuss the effects of desorption. Finally we will discuss other parameters related to the reservoir and the porous medium.

All results are presented in dimensionless form. The conventions for dimensionless time and dimensionless rate used in this work are

$$t_D = 0.0002637 \frac{k}{\phi \mu c_t x_f^2} t \quad \text{.....(3.2)}$$

and

$$q_D = 141.2 \frac{B\mu}{kh(p_i - p_{wf})} q \quad \text{.....(3.3)}$$

This convention is adopted to better enable the identification of those variations in performance which are a consequence of fracture interference, which is the focus of this work.

We also provide rate integral and rate integral-derivative auxiliary functions to illustrate characteristic behaviors (Ilk *et al*. 2007). The rate integral function is defined in Eq. 3.4 as:

$$q_{Ddi}(t_{Dd}) = \frac{1}{t_{Dd}} \int_0^{t_{Dd}} q_{Dd}(\tau)\, d\tau \quad \text{.....(3.4)}$$

and the rate integral-derivative function defined in Eq. 3.5:

$$q_{Ddid}(t_{Dd}) = t_{Dd} \left| \frac{d}{dt_{Dd}} q_{Ddi}(t_{Dd}) \right| \quad \text{.....(3.5)}$$

These functions possess many useful properties when used for diagnosis of production behavior. In this work, we are specifically interested in the property that the rate integral and rate integral-derivative functions for a given system will approach one another when flow boundaries are encountered by the pressure transient, and the functions will merge upon boundary dominated flow.

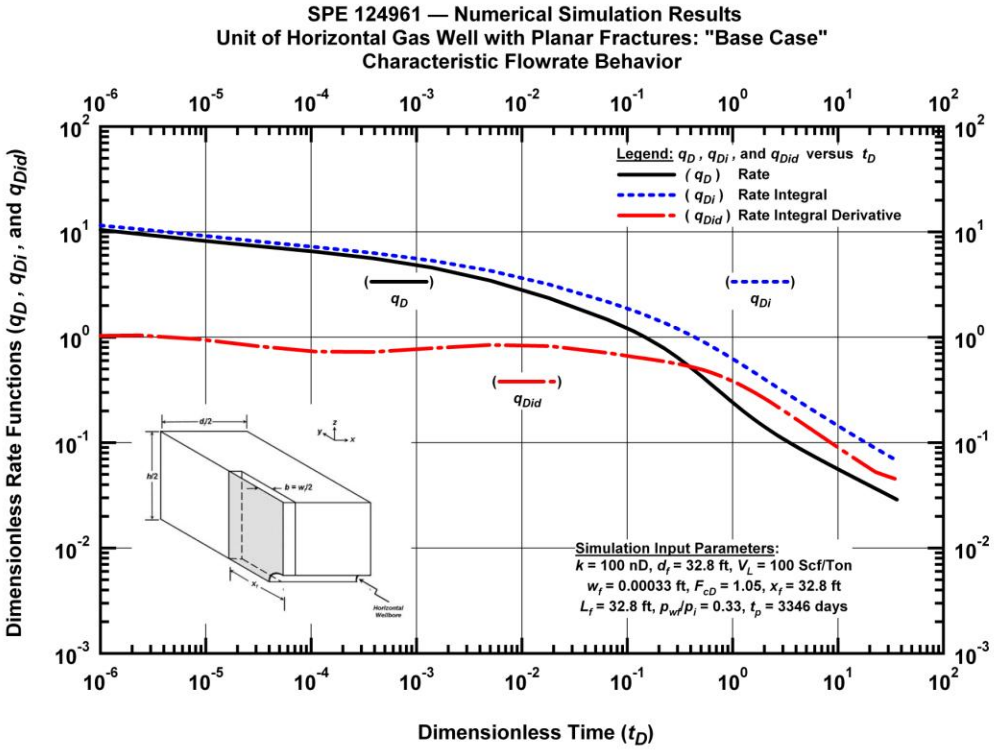

Figure 3.3 — Horizontal gas well with multiple (transverse) fractures: Base case parameters and results.

3.2.1 Base Case Results

The base case simulation parameters were chosen to best represent a typical shale gas reservoir and completion. There exist a broad range of shale plays and a variety of workable completion schemes, but these parameters should provide an acceptable starting point of comparison for any given play. We observe in **Fig. 3.3** the evolution of formation linear flow starting at early times. As the dimensionless time approaches 1, fracture interference comes into effect, and the transition toward compound linear flow is marked by the approach of the rate integral and rate integral derivative functions. However, we note that these two auxiliary functions never actually merge or cross, because no true reservoir boundary exists.

3.2.2 Effect of Complex Fractures

While in some cases there may exist perfectly linear, planar induced fractures, it is possible that a complex yet narrow region of fractured reservoir is created in a fracture treatment. We model this as the occurrence of several parallel planar fractures over a small interval of horizontal wellbore. We observe in **Fig. 3.4** that the presence of a more extensive group of planar fractures results in an increase in early time rate, but that the rates merge at the start of transition from formation linear flow to compound linear flow. The rate

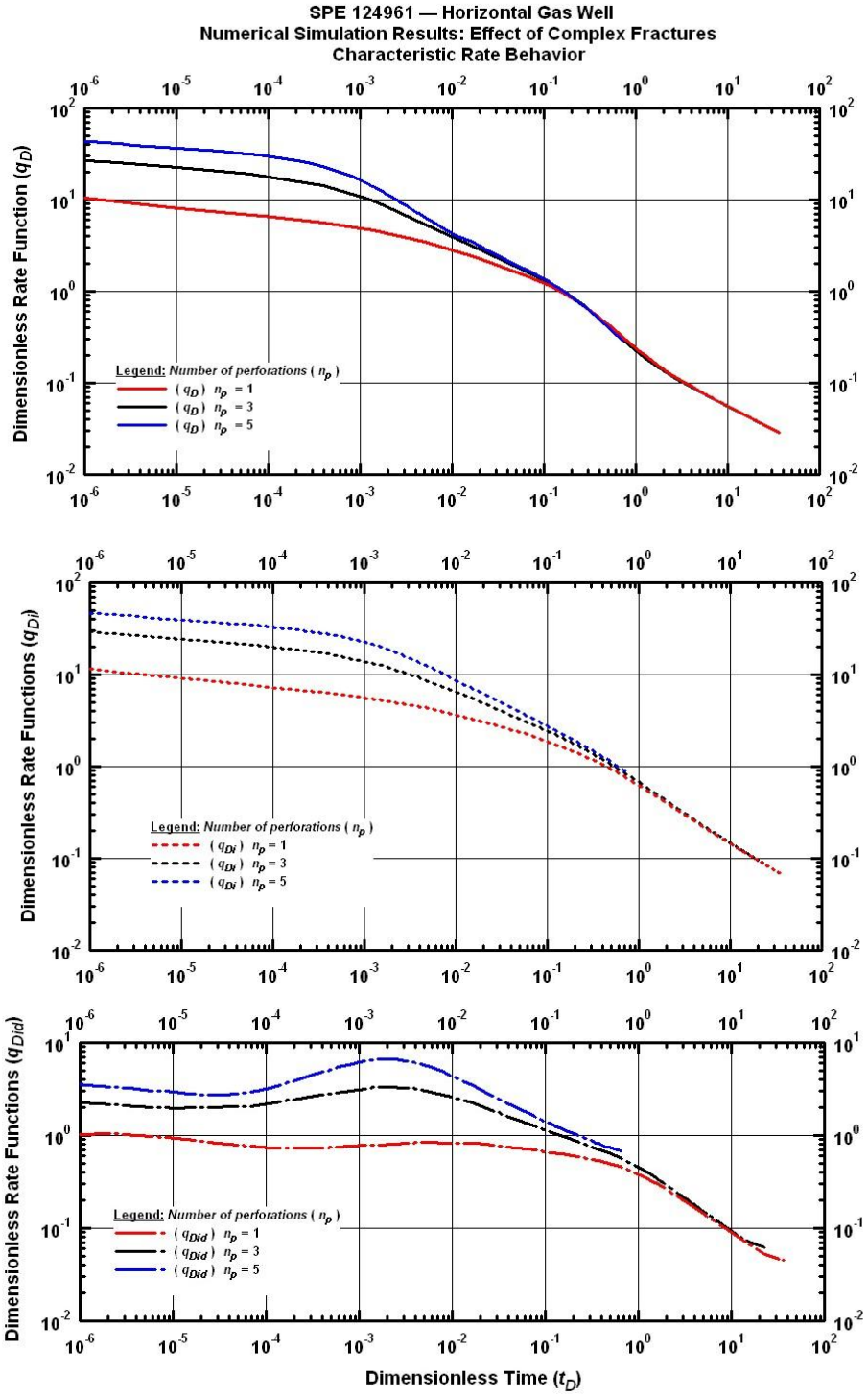

Figure 3.4 — Horizontal gas well with multiple (transverse) fractures: Effect of complex fractures, sensitivity analysis, rates and auxiliary functions.

data for all three cases has clearly merged completely by a dimensionless time of 0.1, which is equivalent to 90 days. In **Fig. 3.4** we are able to see that all the auxiliary functions have the same merging behavior. We can conclude from this observation that that late time behavior of a hydraulic fracture which is complex or branching will not be any different from the behavior of a single planar hydraulic fracture. However, the extent of complexity of the fractures will strongly affect early time behavior, in the case of these results increasing early time rate by a factor of 4 or more.

3.2.3 Effect of Fracture Spacing

We observe the boundary-like effect of fracture interference by comparing runs which vary only in fracture spacing. The data is normalized on a per-fracture basis, and does not reflect the fact that a given horizontal well with tighter fracture spacing will possess a larger number of fractures.

The signature of fracture interference is identified by a substantial drop in flowrate and a corresponding positive slope on the normalized rate-derivative curve. This marks the effective end of linear flow and the beginning of the transition toward compound linear flow, seen very clearly by comparison in **Fig. 3.5**. We can also observe that the rate function and rate integral derivative function appear to cross over during the transition compound linear flow. This effect is clearly illustrated in **Fig. 3.5,** where the normalized rate derivative functions for simulated cases of varying fracture density — approaching the limiting case of stimulated reservoir volume gridding. This auxiliary plot can be used to help identify the onset of "compound-linear" flow. This behavior can easily be mistaken as a reservoir boundary.

A further demonstration of this effect is emphasized in **Fig. 2.1** where we present a comparison of two simulations; the first is the case of a finite reservoir (rectangular boundary), while the other case is an effectively infinite reservoir (no boundary effects are observed). In this figure we observe similar trends for the bounded and unbounded reservoir cases, until boundary effects dominate the response. Wee have imposed a half-slope power-law straight line (representing formation linear flow) — where we note that this trend would (obviously) overestimate future rates after fracture interference begins.

We illustrate the typical system responses that could occur during the production of a horizontal well with multiple fractures in **Fig. 2.1** — at early times, only flow from fractures is observed corresponding to formation linear flow, this flow regime is identified by the half-slope. Then fracture interference effects are being felt which corresponds to a transitional flow regime. Next, we observe the "compound linear flow regime" and finally flow regime becomes elliptical. The small icons in this figure visually depict the flow regimes of linear, compound linear, and beginning elliptic flow.

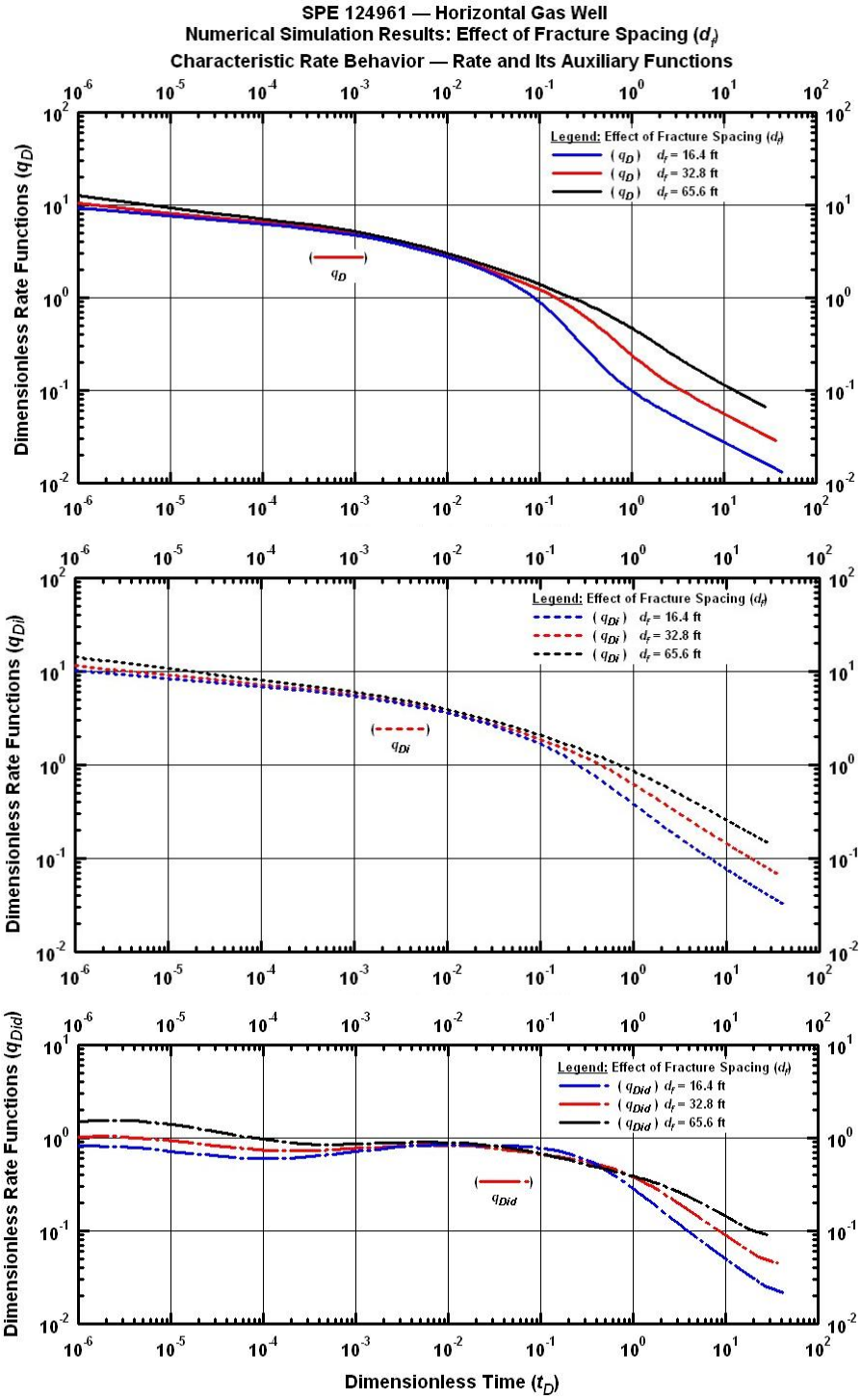

Figure 3.5— Horizontal gas well with multiple (transverse) fractures: Effect of fracture spacing, sensitivity analysis, rates and auxiliary functions.

3.2.4 Effect of Fracture Conductivity

The clearest indication of change to the performance behavior is seen in the very early time. The four cases shown in **Fig. 3.6** correspond to different equivalent fracture widths, and directly to different fracture conductivities, ranging from extremely low to extremely high. We see from these figures that the contribution from the fracture is greater at earlier time, and the steepness of decline is less severe in the cases with less fracture conductivity. In middle-time ranges it is observed that the rates of the higher-conductivity stems begin to merge. The higher-conductivity fracture aggressively evacuates the near-fracture region but production soon becomes dominated by the low permeability of the matrix. Rate becomes dominated by fracture surface area rather than fracture conductivity.

We see from **Fig. 3.7** that the pressure depletion near the fracture face is very severe as indicated by the steepness of the pressure profile. With the very low-conductivity, thinner fracture, the wellbore inflow effect is more dominant in the production data signature. In these low-conductivity cases it is difficult to identify a clear half-slope linear flow period. Real wells with ineffective fracture treatments will display more dominant signature horizontal well flow effects and less distinct linear flow effects. No fracture interference effects are observed through this time interval.

Note that the general observations regarding the *effect of complex fractures* and the *effect of fracture conductivity* are similar. A fracture which possesses a higher conductivity or a greater complexity will exhibit a higher initial rate, while ultimately the rate behavior will merge with cases with lower fracture conductivity or fracture complexity. It is doubtful whether the relative effects of fracture complexity and fracture conductivity will be extricable or identifiable.

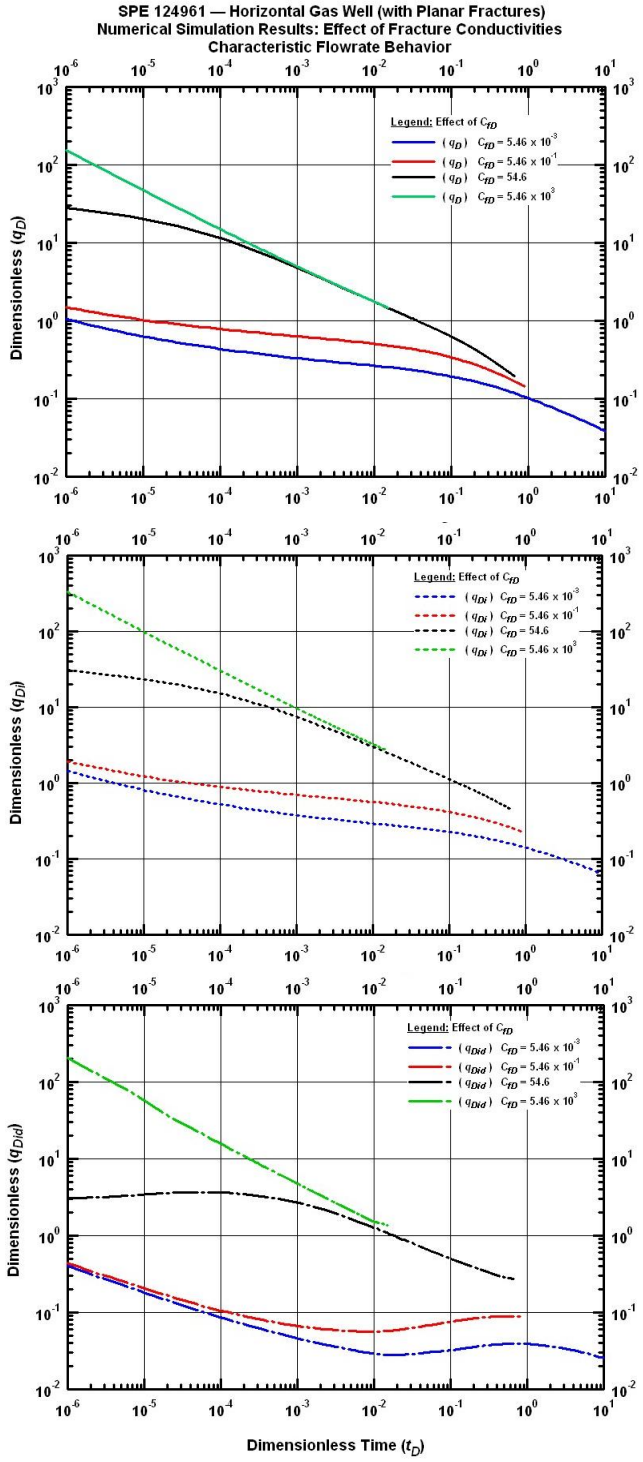

Figure 3.6 — Horizontal gas well with multiple (transverse) fractures: Effect of fracture conductivity, sensitivity analysis, rates and auxiliary functions.

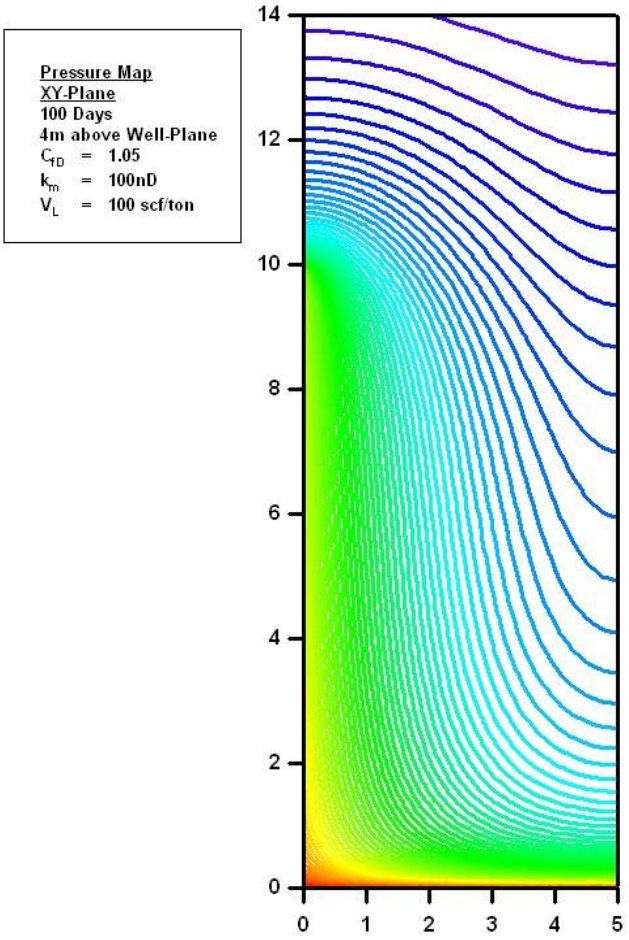

Figure 3.7 — Pressure map showing pressure depletion at 100 days into production, aerial view.

3.2.5 Effect of Desorption

The next observation concerns the apparent effect of varying desorptive contribution. **Fig. 3.8** clearly shows the increase in rate and the lengthening of the rate forward in time that accompanies higher desorptive contribution, effectively changing the energy of the system. The first apparent effect is that greater sorptive storage yields higher rates; the second effect is that the pressure profile is steeper as it propagates away from the fracture, as visually depicted in the pressure map, **Fig. 3.7**. Pressure does not correspond linearly to mass storage, since the sorption isotherm is highly nonlinear. As such, we visualize in **Fig. 3.9** the dimensionless mass of gas found at various distance intervals from the hydraulic fracture.

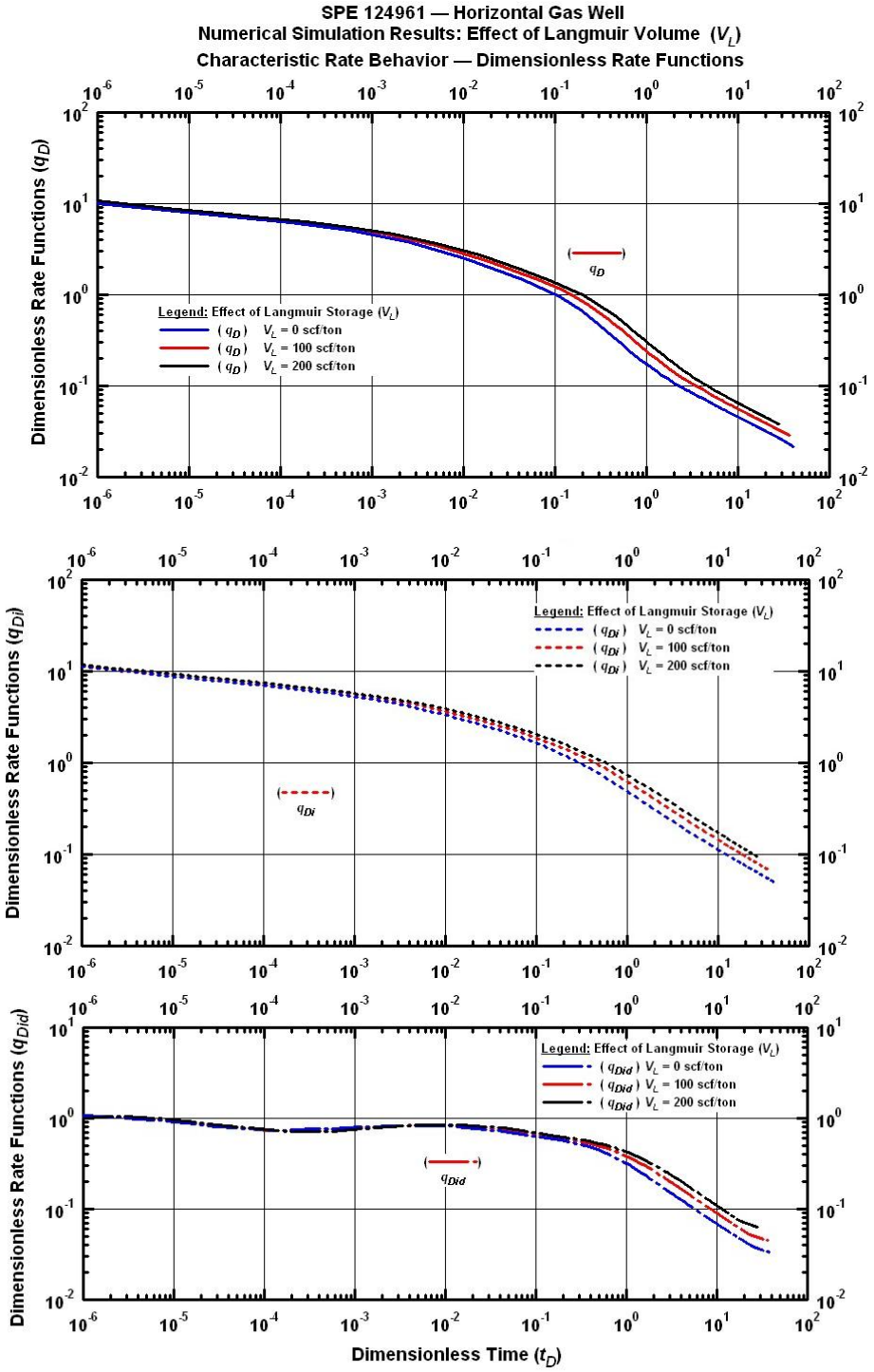

Figure 3.8 — Horizontal gas well with multiple (transverse) fractures: Effect of Langmuir storage, sensitivity analysis, rates and auxiliary functions.

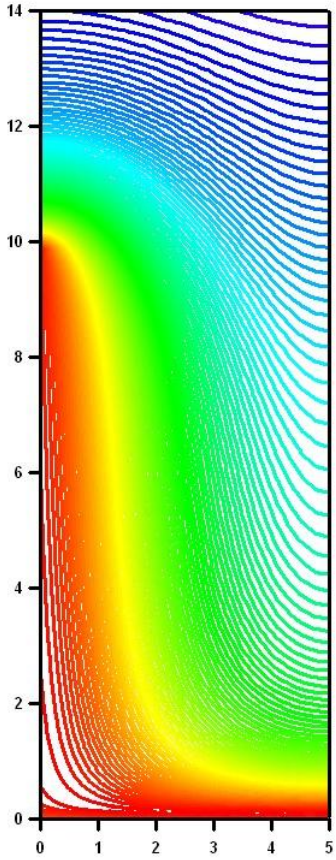

Figure 3.9 — Sorption map showing steepness of sorption gradient at 100 days into production, aerial view.

The purpose of this figure is twofold – one, to show how slowly the pressure transient moves outward and how thoroughly it depletes a region of gas before advancing, and two, to show how much residual gas remains even after the pressure is drawn down to near wellbore flowing pressure. Further, **Fig. 3.9** lets us examine the steepness and near-fracture localization of the depletion from surface sorption. This emphasizes the steepness of the pressure front due to the ultra-low permeability.

There currently exists no method by which to account for desorption in the nondimensionalization since there is no satisfactory general analytical solution featuring desorption. Since desorption responds to pressure in a nonlinear fashion, and desorption is more properly characterized by at least two parameters (Langmuir volume and Langmuir pressure,) it is not strictly appropriate to scale the results by any

constant. However, we obtain interesting results by altering the dimensionless time definition to include an arbitrary variable characterizing sorptive energy.

$$t_D = 0.0002637 \frac{k}{\phi \mu c_t x_f^2} \frac{1}{[1+(0.00525)V_L]} t \quad \text{.....(3.6)}$$

The Langmuir volume term is frequently treated as being dimensionless in mathematical developments of desorption. The constant 0.00525 may hold a physical significance (i.e. it may correspond to a unit conversion factor and/or another reservoir parameter) but determination of its meaning will be the goal of future work. Using the adjustment in Eq. 3.6, we show in **Fig. 3.10** that scaling the dimensionless time by a constant factor appears to completely normalize for the effect of desorption. Observing **Fig. 3.10** and comparing it with **Fig. 3.8**, it can be verified that desorption delays the effect of fracture interference when we compare the normalized desorption signatures with the true effect of fracture interference caused by varying fracture spacing.

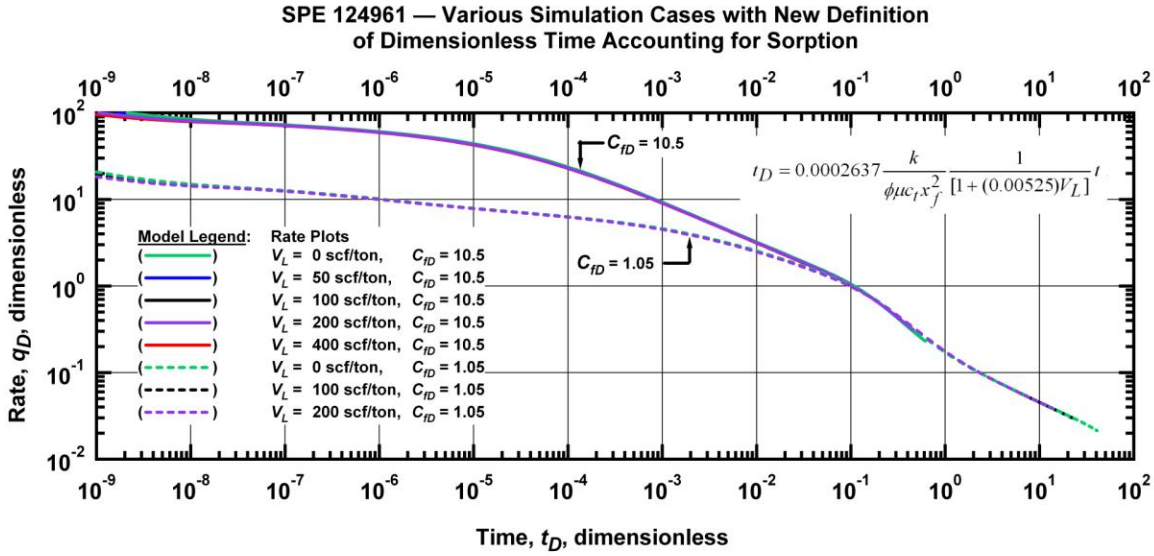

Figure 3.10 — Horizontal gas well with multiple (transverse) fractures: Effect of desorption, redefined dimensionless time parameter normalizing for Langmuir volume.

3.2.6 Effect of Matrix Permeability

The next observation concerns the apparent effect of varying the matrix permeability. **Fig. 3.11** shows the effect of varying matrix permeability from a very small value of 10nd to a value of 1 md.

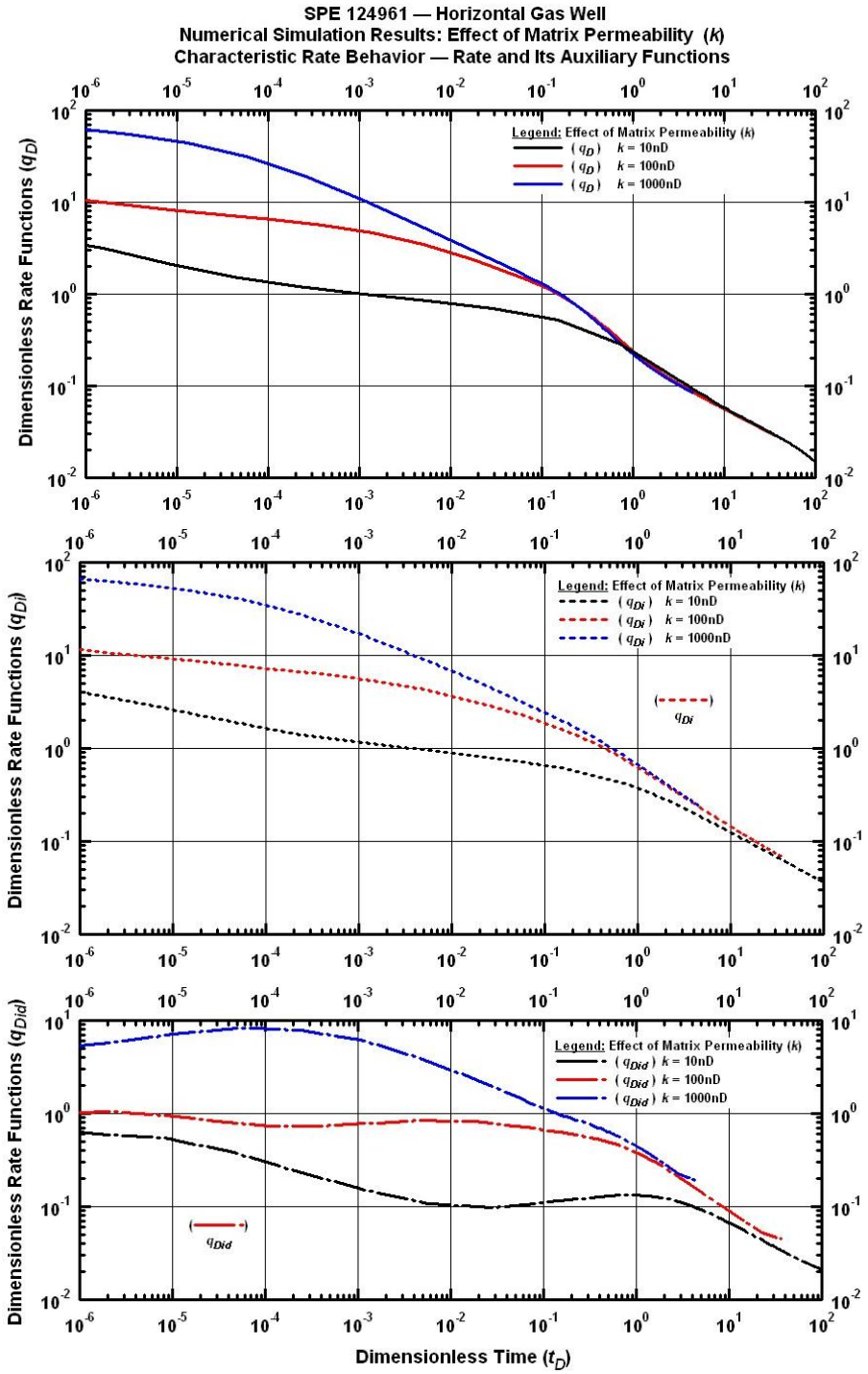

Figure 3.11 — Horizontal gas well with multiple (transverse) fractures: Effect of matrix permeability, sensitivity analysis, all rates.

Matrix permeability appears to affect early time behavior in particular. Convergence of the rate profiles is observed at late times, in particular during compound linear flow. Again, it is noteworthy that varying permeability appears to strongly affect early time rate data while the rate behavior merges at late times. However, it must be emphasized that permeability is a term in the nondimensionalization of both rate and time. Consequently, this behavior would not appear in rate-time data prior to nondimensionalization. The outstanding result is that nondimensionalization with respect to permeability does not cause the three rate curves to overlie one another. This is due to the complex evolution of the pressure profiles over time through the asymmetric near-wellbore reservoir geometry.

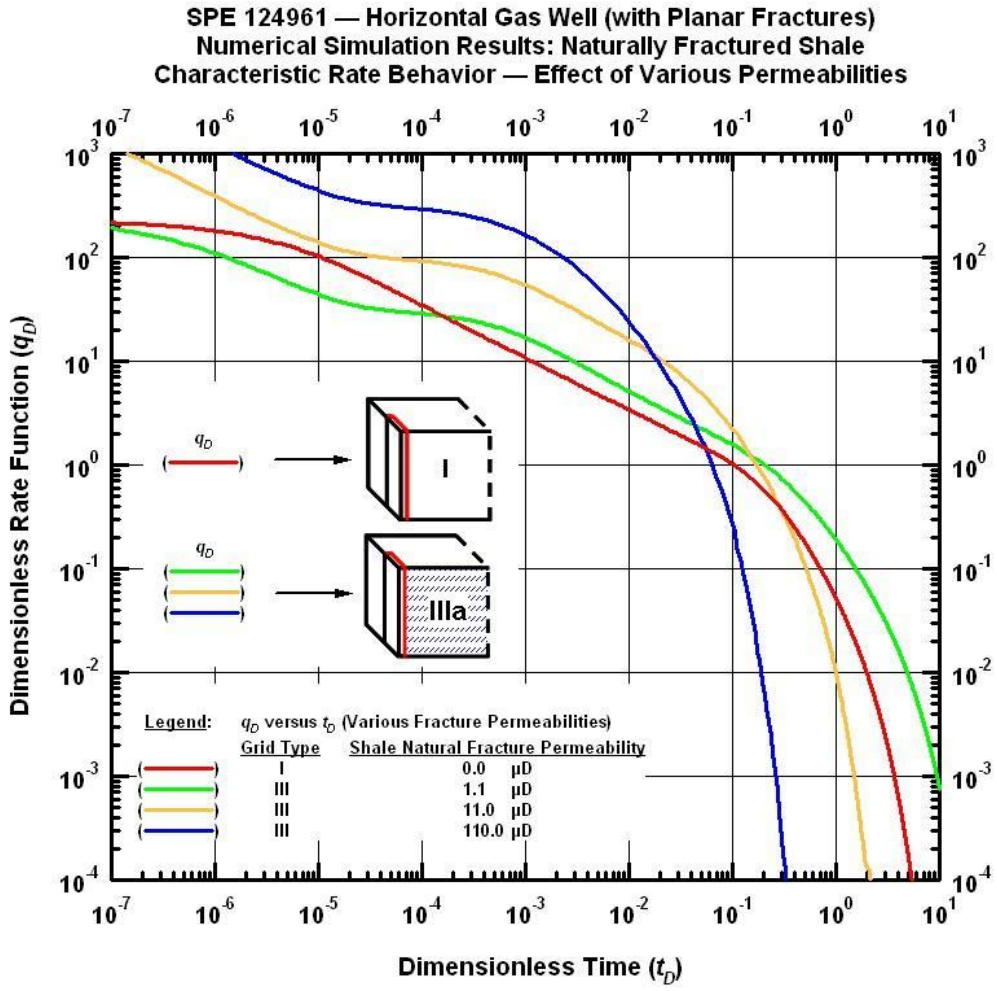

Figure 3.12 — Induced fracture system: Effect of natural fractures with various fracture system permeabilities, sensitivity analysis, rates only.

3.2.7 Effect of Natural Fractures

The presence and influence of natural fractures in tight gas and shale gas reservoir systems is a matter of debate. Likewise, the role of complex induced fracture networks is not fully understood and its characterization remains a matter of conjecture. We illustrate possible configurations of in situ fracture orientations in **Fig. 2.1**. We model the effect of a natural or complex induced fracture network by using a dual porosity model with various shale fracture network permeabilities. As shown in **Fig. 3.12**, the presence of conductive natural or induced fractures leads to a higher initial rate but overall a much shorter or nonexistent linear flow period, and faster depletion.

We attempt to capture the possibility that the fracture treatment creates or re-activates a region around the induced planar hydraulic fracture. We model this by treating the region near the induced fracture by a dual porosity model with conductive natural fractures, while the region more distant from the induced fracture is unstimulated shale of 100nd permeability.

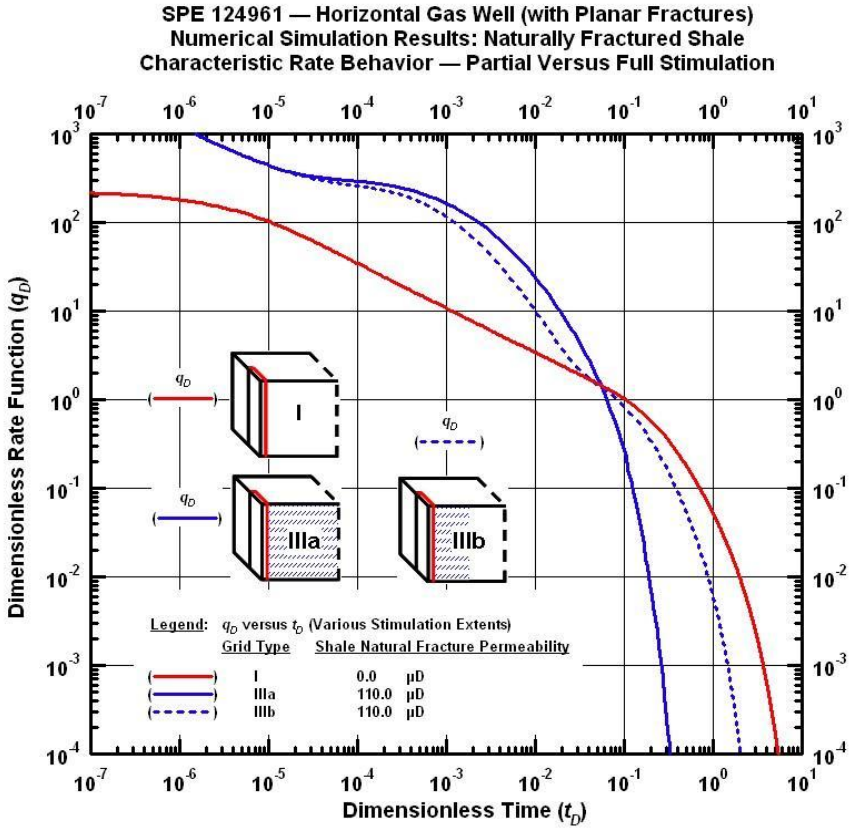

Figure 3.13 — Induced fracture system: Effect of discontinuous fracture networks, sensitivity analysis, rates only.

In **Fig. 3.13** we demonstrate that Case IIIb (corresponding to a near-fracture stimulated region) exhibits flow features from both the base case of a single planar fracture (Case I) and the limiting case, Case IIIa, representing a fully fractured reservoir. In fact, an inflection point in the rate behavior of Case III occurs at the exact point of intersection of Case I and Case IIIa.

3.2.8 Effect of High-Conductivity Layers

Core samples of shale gas reservoirs reveal a large degree of stratification and the likely presence of higher-conductivity layers. A possible layout of this system is illustrated in Case IIa and Case IIb in **Fig. 2.1**. Fracture stimulation may further fracture already brittle layers, such as microlayers of carbonate sediment.

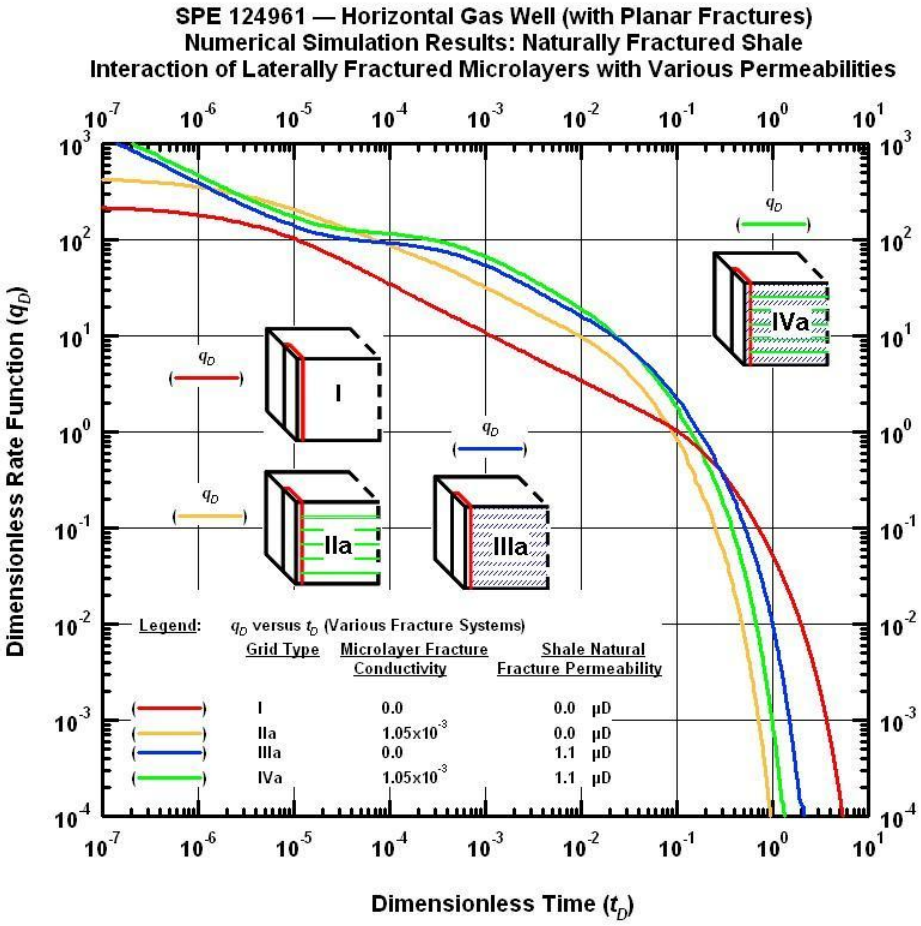

Figure 3.14 — Induced fracture system: Effect of laterally continuous high conductivity layers and interaction with natural fracture system, sensitivity analysis, rates only.

Microseismic monitoring of fracture treatments indicates that microseismic events occur in a ‘cloud’ around the perforations. The distribution and extent of the cloud vary depending on the geology and the stimulation treatment design.

In **Fig. 3.14** we compare the behavior of reservoirs with high-conductivity layers (Case IIa) against a naturally-fractured or complex-fractured reservoir (Case IIIa) and finally a reservoir possessing both natural fractures and laterally continuous high conductivity layers (Case IVa.) All these results are compared, once again, against the base case (Case Ia) possessing only a single vertical fracture. We observe that late time behavior shows the same character, regardless of the fracture configuration, indicating that at late times, the signature of laterally continuous layers may be indistinguishable from a natural fracture signature. However, at early times, systems possessing natural fractures show a strong fracture-depletion signature which does not occur in the case with laterally continuous layers.

3.3 Conclusions

In this work we make an attempt to characterize the influence of various reservoir and completion parameters on performance of multiply-fractured horizontal wells in ultra-low permeability reservoir systems.

Contrary to intuition, the effect of desorption can be accounted for by a time scaling constant. The presence of desorption appears to shift fracture interference forward in time.

Ultra-low permeability systems with large fractures will possess extremely sharp pressure gradients. The steepness of these gradients will be exacerbated where desorption is present. The onset of fracture interference is gradual and flow regimes in these systems are constantly evolving. The use of coarse gridding schemes will fail to capture the nuance of this evolution and will lead to inaccurate characterization of fracture interference behavior, as well as inaccurate interpretation of production data.

While a dual porosity model may appear to fit real data, such a model will not correctly capture the effect of fracture interference. Fracture interference is an inescapably transient effect which appears to approach boundary-dominated flow but never reaches it. None of these three features/observations is a true reservoir boundary. Due to the relatively small volumes of investigation of these well systems, it is unlikely that reservoir compartmentalization is the true cause of "boundary-dominated flow" effects as interpreted from rate data.

The features of higher permeability, higher fracture conductivity, higher induced fracture complexity, and more highly fractured reservoir will all lead to a higher initial rate and initial dimensionless rate, yet late time dimensionless rates will merge with lower permeability/conductivity/complexity cases sometime during the compound linear flow period. The effect of desorption, on the other hand, is more apparent at late time than early time, tending to prolong all flow periods and extend production.

CHAPTER IV

DEVELOPMENT AND VALIDATION OF MICROSCALE FLOW

This appendix presents the derivation and validation of the method for computing diffusive and mean free path parameters in this work. These parameters are used to compute molecular diffusion and apparent permeability in the numerical model as a function of pressure and composition.

Section 4.1 describes the Florence *et al*. (2007) equation for computation of apparent permeability to gas accounting for microflow effects. Section 4.2 develops the multicomponent mean free path computation. Section 4.3 discusses the development of an average velocity for a species in a gas mixture. Section 4.4 develops a method for estimation of diffusivity using the mean free path and microflow parameters, and verifies the method against measured data and against other established methodologies.

4.1 Florence Microflow Equation

Klinkenberg (1941) demonstrated the approximately linear relationship between measured permeability and inverse pressure:

$$k_a = k_\infty \left[1 + \frac{b_K}{p} \right] \quad \text{.....(4.1)}$$

where k_a is the apparent or measured permeability to gas in m^2 while k_∞ is the calculated permeability at infinite pressure in m^2. The constant b_K is an empirically measured term called the Klinkenberg constant, in units of Pa (Klinkenberg 1941). The gas slippage factor is regarded as constant in the flow regime where the Klinkenberg approximation is valid, and is related to the mean free path

$$\frac{b_K}{p} = \frac{4c\lambda}{r_{pore}} \quad \text{.....(4.2)}$$

where c is a constant approximately equal to 1 and r_{pore} is an effective pore radius. This gas slippage factor is related to the beta term via

$$b_K = \beta \left[\frac{k_\infty}{\phi} \right]^{-0.5} \quad \text{.....(4.3)}$$

where the β term serves as another parameter to be used in correlating Klinkenberg constant with porosity and permeability in units of Pa, and ϕ is the measured sample porosity (Civan 2008). While this beta-form of the Klinkenberg approximation is simple and convenient for the purposes of numerical simulation due to its computational simplicity, it is not valid for very small pores, it treats the gas as a bulk phase with no dependence on species, and it requires two empirical, measured constants. A more robust, rigorously developed "microflow" model has been proposed by Florence, *et al*. (2007), which is valid for all flow regimes in porous media, from free-molecular flow through continuum flow, though not verified and

probably invalid in high-rate inertial (Forchheimer) flow regimes. The basis of this model is to adjust the theoretical permeability to an 'effective' permeability through use of only the Knudsen number and the permeability at infinite pressure.

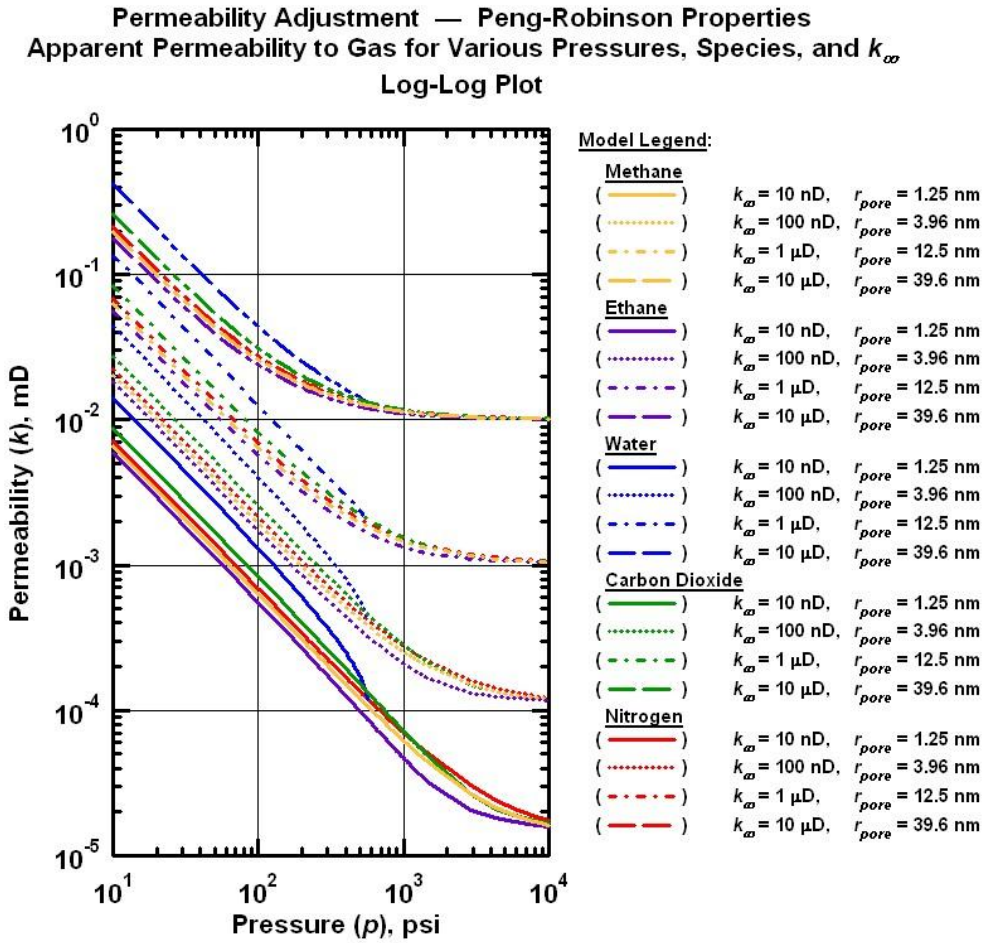

Figure 4.1 — The Florence model (Eq. 3.4) is used to compute apparent permeabilities. For low pressures, apparent permeability to gas is enhanced by several orders of magnitude compared to the permeability to liquid (k_∞) while for higher pressures, which typical tight gas and shale gas reservoirs might be assumed to occupy, still exhibit significant permeability enhancement. The permeability enhancement is strongly dependent on the gas species.

The Florence, *et al.* (2007). microflow equation expresses the apparent permeability as:

$$k_a = k_\infty [1+\alpha(Kn)Kn]\left[1+\frac{4Kn}{1+Kn}\right] \quad \text{.....(4.4)}$$

The function α is a rarefaction coefficient parameter, a dimensionless adjustment parameter of the form

$$\alpha(Kn) = \alpha_0 \frac{2}{\pi}\tan^{-1}\left[c_1 Kn^{c2}\right] \quad \text{.....(4.5)}$$

where c_1 is a constant valued at 4.0, c_2 is a constant valued at 0.4, and α_0 is a constant valued at $64/(15\pi)$. If the species-dependent Knudsen number is used then the microflow formula, Eq. 4.4, will vary the apparent or effective permeability experienced by each individual gas species, due to the fact that each gas species in the mixture will have a different mean free path (as computed by Eq. 4.11) and thus a different Knudsen number. Implementation of this theory enables modeling of the fractionating effect of reservoirs with extremely small pores, wherein smaller molecules flow preferentially faster than larger ones. **Fig. 4.1** shows the impact of various pore throat dimensions on adjusted permeability for various gases.

The Knudsen number is a dimensionless parameter which characterizes the degree to which flow will be affected by the medium through which it passes, typically either porous media or capillary tubes, and is defined by Eq. 3.6:

$$Kn = \frac{\bar{\lambda}}{l_{char}} \quad \text{.....(4.6)}$$

Where λ is the mean free path defined in Section 3.2. The value of l_{char}, the characteristic feature scale, corresponds to capillary tube radius (Karniadakis and Beskok 2001) and is analogous to an average effective pore throat radius in porous media. The relation in Eq. 4.7 estimates the average effective pore throat radius,

$$r_{pore} = l_{char} = 8.85\times10^{-6}\sqrt{\frac{k_\infty}{\phi}} \quad \text{.....(4.7)}$$

where r_{pore} corresponds to the average pore throat radius in cm, l_{char} is the characteristic length of the medium in cm, k_∞ is the permeability to liquid or alternatively the permeability at infinite pressure in md, and ϕ is the porosity in fraction.

This effective pore throat radius value serves as a characterization of the porous media. It may or may not necessarily correspond to a literal average pore throat radius. It simply provides a parameterization we can use to compute the Knudsen number.

Due to each species having a different apparent permeability, porous media with extremely fine pores will have a tendency to fractionate the gas into its components. It is important to simultaneously implement concentration gradient-driven diffusion as developed in Section 3.4. This honors the natural tendency of gases to intermix and diffuse due to Brownian motion. Correctly accounting for concentration gradient-driven diffusion will tend to blur the concentration gradient and reduce the degree of the microflow effect.

In situations with very low pressure drawdown, Brownian diffusion such as this may be a more significant facilitator of transport than convective flow.

4.2 Development of Mean Free Path

In order to compute the apparent permeability to individual gas species in a gas mixture using Eq. 3.4, it is first necessary to compute an individual Knudsen number for each species and therefore an individual mean free path for each species.

The flow regime of Knudsen flow, similar to the idea of gas slippage, occurs when the mean free path of the gas molecules is on the order of the average pore throat radii. The mean free path of a molecule in a single-component gas can be computed by

$$\bar{\lambda}(p,T) = \sqrt{\pi/2}\,\frac{1}{p}\,\mu\sqrt{\frac{RT}{M}} \qquad (4.8)$$

where, on the left hand side, p is the average pore pressure in Pa and T is temperature in Kelvin. On the right hand side, μ is the gas viscosity in Pa-s, R is the ideal gas constant in m^3-Pa/K-mol, and M is the molecular mass of the gas species in g/mol.

The mean free path of a molecule in a single-component gas is conceptually the ratio of the distance traveled divided by the volume of interaction,

$$\bar{\lambda} = \frac{\text{distance traveled}}{\text{volume of interaction}} = \frac{\bar{v}t}{\pi d_k{}^2 \bar{v} t n_v} \qquad (4.9)$$

where v is the mean velocity in m/s, d is the molecular kinetic diameter (measured in laboratory experiments) in m, n_v is a term related to density indicating number of moles of gas per unit volume measured in mol/m^3, and t is a time-of-flight parameter in s which cancels out.

There exists some contradiction in the literature regarding appropriate values for molecular diameter. For determination of *Kn* in porous media, kinetic diameter is used. Study of transport of zeolites (Chen, Degnan and Smith 1994) reveals that the empirically determined kinetic diameter will depend to some degree on the chemical and physical nature of the porous media used in the testing. In other words, effective molecular diameter may be a function of the *in situ* geochemistry, not only a function of the molecular species. No current method exists to calibrate for this effect, so we use the molecular constants in **Table 4.1** in this work. We leave open the potential for refinement of these constants for given reservoir systems.

Eq. 4.8 can only be applied for a single-component gas or by assuming average gas properties. Eq. 4.8 must be altered for use in a multicomponent gas scenario. First, the formula for average velocity of a species in a multicomponent mixture reduces to simply

$$\overline{v_{rel}} = \sqrt{\overline{v_1}^2 + \overline{v_2}^2} \quad \text{.....(4.10)}$$

where v_1 and v_2 are the average velocities of species (1) and (2), and v_{rel} is the effective relative velocity between the two species. The development of Eq. 4.10 is treated in Section 4.3.

Table 4.1 — Kinetic molecular diameters were obtained from the sources listed. These kinetic diameters were used in mean free path calculations.

Gas	Molar Mass	Kinetic Diameter	Resource for Kinetic Diameter
	M	d_k	
	(g/mol)	(nm)	
Methane	16.043	0.38	(Gupta 1994)
Ethane	30.07	0.4	(Sadakane 2008)
Propane	34.082	0.43	(Collins 1996)
Carbon Dioxide	44.01	0.33	(Sadakane 2008)
Water	18.015	0.265	(Ivanova 2007)
Nitrogen	28.014	0.364	(Collins 1996)

For one gas species in a multicomponent gas mixture, the "volume of interaction" term (the denominator) of the expression is modified, changing the expression to

$$\overline{\lambda}_1 = \frac{\overline{v_1}}{\sum_{j=1,n} \pi d_1 d_j \sqrt{\overline{v_1}^2 + \overline{v_j}^2}\, n_{vj}} \quad \text{.....(4.11)}$$

where the subscript n connotes the total number of species present in the gas phase and λ_1.indicates the mean free path of species (1) only. The terms in this equation representing molecular diameter are the measured kinetic diameters of those gases. The n_{vi} term is a molar density, representing the number of molecules of species i per unit volume, and can be modified by a perfect gas law approximation such that

$$\overline{\lambda}_1 = \frac{\overline{v_1}}{\sum_{j=1,n} \pi d_1 d_j \sqrt{\overline{v_1}^2 + \overline{v_j}^2}\, \frac{N_A p_j}{RT}} \quad \text{.....(4.12)}$$

where N_A is Avogadro's number and p_i is the partial pressure of species i. Rather than relying on a perfect gas assumption, we can use the more accurate computation for density of a gas mixture as a function of pressure, temperature, and composition using the Peng-Robinson equation of state already intrinsic to our numerical implementation. Thus we substitute this computed density into Eq. 4.12 to yield:

$$\bar{\lambda}_1 = \frac{\bar{v}_1}{\sum_{j=1,n} \pi d_1 d_j \sqrt{\bar{v}_1^2 + \bar{v}_j^2}\, \frac{N_A \rho X_j}{M_j}} \quad \text{.....(4.13)}$$

where ρ is our correct (Peng-Robinson[5]) density of the gas phase accounting for nonlinearities in gas mixing and X_i is the dimensionless mass fraction of species i in the gas phase.

We now have a method by which to characterize the mean free path length of any individual gas species in the multicomponent gas within our system. Thus we can now examine the ramifications of different mean free paths on gas flow in porous media with microscale features. The dimensionless Knudsen number will determine the severity of the non-Darcy 'microflow' effect.

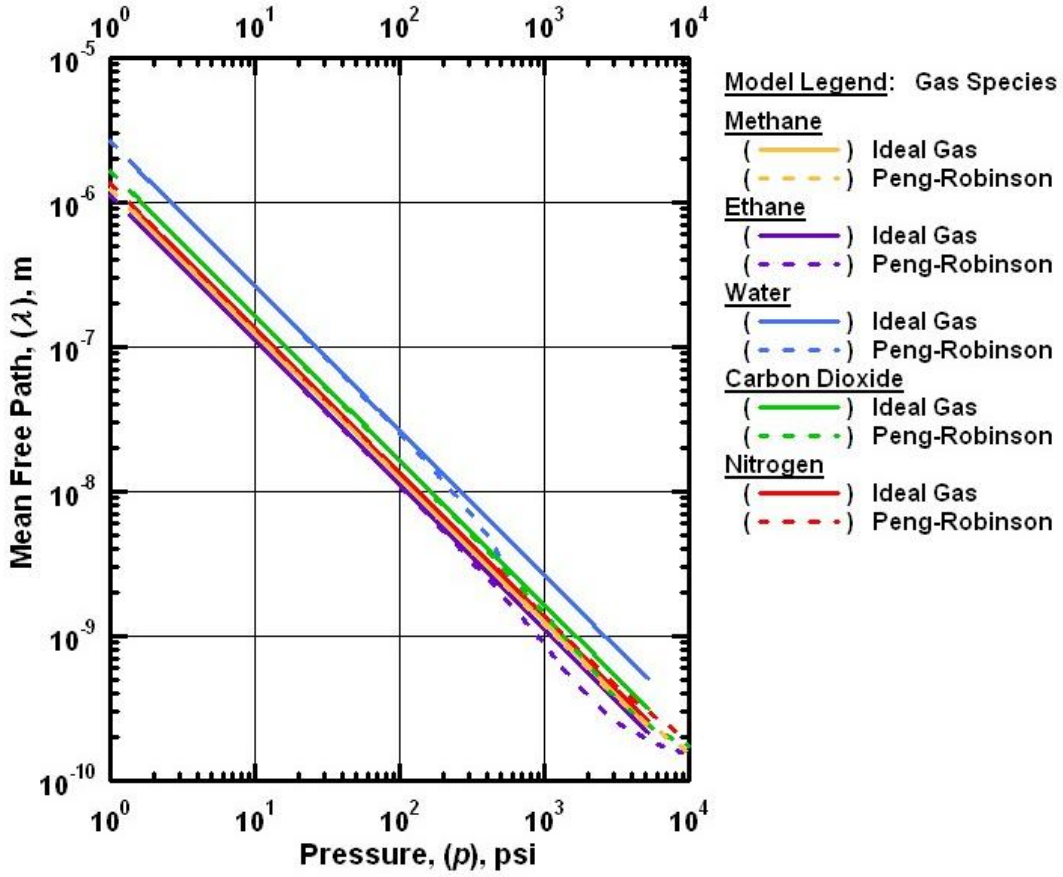

Figure 4.2 — Mean free path decreases with increasing pressure. Lighter gas species possess longer mean free path for a given pressure, barring nonlinearities. Deviation from a straight-line trend is due to the computation of mean free path by means of Eq. 3.13, incorporating the density computed by the Peng-Robinson equation of state.

There exists insufficient available data on measured mean free path values in gas mixtures to validate Eq. 4.13 explicitly, Section 4.4 we attempt to validate the accuracy of 4.11 through indirect computation of the diffusivity coefficient for gases. **Fig. 4.2** demonstrates the effect of pressure on mean free path for various gases.

4.3 Development of Molecular Velocity in a Gas Mixture

Eq. 4.6 can only be applied for a single-component gas, and thus must be altered for use in a multicomponent gas scenario. We rewrite the mean free path to account for multiple gas species, first accounting for average velocity. The average velocity of a molecule in a single component gas[35] is

$$\bar{v} = \sqrt{\frac{8RT}{\pi M}} \quad \text{.....(4.14)}$$

The use of a single average velocity is inappropriate for a gas mixture, where each species in the gas possesses a different average velocity as a function of molar mass. Therefore, we must compute the average velocity of a gas molecule in a gas mixture.

The relative velocity, v_{rel}, between two gas particles is expressed as

$$v_{rel} = \sqrt{\vec{v}_{rel} \cdot \vec{v}_{rel}} \quad \text{.....(4.15)}$$

where the relative velocity vector between two molecules of different species can be expressed as

$$\vec{v}_{rel} = \vec{v}_1 - \vec{v}_2 \quad \text{.....(4.16)}$$

So, taking the magnitude of the relative velocity vector,

$$v_{rel} = \sqrt{(\vec{v}_1 - \vec{v}_2) \cdot (\vec{v}_1 - \vec{v}_2)} \quad \text{.....(4.17)}$$

Rearranging Eq. 3.17, we obtain:

$$v_{rel} = \sqrt{\vec{v}_1 \cdot \vec{v}_1 - 2\vec{v}_1 \cdot \vec{v}_2 + \vec{v}_2 \cdot \vec{v}_2} \quad \text{.....(4.18)}$$

Since we are not truly examining individual molecules but rather the average properties of the statistical ensemble of the gas, we take the averages of the terms

$$\overline{v_{rel}} = \sqrt{\overline{\vec{v}_1 \cdot \vec{v}_1} - 2\overline{\vec{v}_1 \cdot \vec{v}_2} + \overline{\vec{v}_2 \cdot \vec{v}_2}} \quad \text{.....(4.19)}$$

Since $\overline{\vec{v}_1}$ and $\overline{\vec{v}_2}$ (the average velocity vectors for two different gas particles) are random and uncorrelated, their dot product equals zero. Thus the formula for average velocity reduces to simply

$$\overline{v_{rel}} = \sqrt{\overline{v_1}^2 + \overline{v_2}^2} \quad \text{.....(4.20)}$$

where the average velocities of the species (1) and (2) are different, each having been computed from Eq. 4.14 independently.

4.4 Development and Validation of Diffusion and Mean Free Path Methodology

Because we now are dealing with concentration gradients as well as pressure gradients, it is not appropriate to neglect molecular diffusion. In diffusive flow, the driving force is the concentration gradient. Using the microflow permeability correction without accounting for the gradient-blurring effect of molecular diffusion would yield incorrect results. The mass flux due to molecular diffusion[2] is

$$J_i = -\phi S_G(\tau_G)\delta D_{G,i}\rho_G \nabla X_{G,i} \quad (4.21)$$

where the vector J_i is the molar flux, S_G is the gas saturation is fraction, τ_G is the tortuosity computed by the Millington and Quirk (1961) in fraction, δ is the constrictivity in fraction, which is a function of the ratio of the molecular radius to the average pore radius, $D_{G,i}$ is the diffusion coefficient of species i in the gas phase in m^2/s, ρ_G is the density of the gas phase computed by the Peng-Robinson equation of state, and the gradient of $X_{G,i}$ is the mass fraction of species i in the gas phase.

Tortuosity is computed by the Millington and Quirk (1961) model,

$$\tau_G = \phi^{1/3} S_G^{7/3} \quad (4.22)$$

The diffusivity can be estimated from kinetic theory of gases. When possible, empirical data should be used for diffusivities; however, due to the expectation of complex gas mixtures for which data is unavailable, a derived kinetic theory approximation must suffice. The expression for approximating the diffusivity of a pure gas (self-diffusion) from kinetic theory principles (Bird, Stewart and Lightfoot 2007) is

$$D_{11} = \frac{1}{3}\sqrt{\frac{8k_BT}{\pi M}}\frac{k_BT}{\sqrt{2}\pi d^2 p} \quad (4.23)$$

where k_B is Boltzmann's constant of $1.3806503 \times 10^{-23}$ in units of m^2-kg/(s^2-K). Clearly this method assumes ideal gas kinetics. This is identical to

$$D_{11} = \frac{1}{3}\bar{v}\bar{\lambda} \quad (4.24)$$

For a multicomponent gas, we extend our derivation of the mean free path for a multicomponent gas,

$$D_1 = \frac{1}{3}\bar{v}_1\bar{\lambda}_1 \quad (4.25)$$

In the case where the pore throat dimensions are smaller than the mean free paths of a given species, the pore throat radius can be used in lieu of the mean free path. Recall our computation for the mean free path of a species in a gas mixture, Eq. 3.13. Substituting Eq. 3.13 into Eq. 3.25,

$$D_1 = \frac{1}{3}\overline{v_1}\frac{\overline{v_1}}{\sum_{j=1,n}\pi d_1 d_j \sqrt{\overline{v_1}^2 + \overline{v_j}^2}\,\frac{N_A \rho X_j}{M_j}} \quad \text{.....(4.26)}$$

Note that Eq. 3.26 for the diffusivity constant is only valid for the case where the molecule can be expected to traverse the mean free path without encountering an obstacle. It is not valid for Knudsen flow or any other flow regime where the molecules are expected to encounter the pore walls. Thus the parameters of the porous media are used to scale the diffusivity coefficient, via

$$D_{1,pore} = D_1 S_G \delta \tau_G \phi \quad \text{.....(4.27)}$$

where δ is the constrictivity, which accounts for the interactions of the molecules with the pore walls when the molecular diameter is on the same order as the pore throat diameter.

Constrictivity is typically treated as a purely empirical descriptive parameter, so no robust formulation for its estimation exists. Lacking any superior functional definition of constrictivity, we have developed Eq. 3.28 to approximate the character of its effects:

$$\delta_i = 1 - \frac{d_i}{2r_{pore}} \quad \text{.....(4.28)}$$

In **Table 4.2** we examine the results of this formulation in predicting the self-diffusion coefficient of methane in comparison to experimentally measured values and the Chapman-Enskog (Chapman and Cowling 1991) equation,

$$D_{AB} = 0.0018583\sqrt{T^3\left[\frac{1}{M_A} + \frac{1}{M_B}\right]}\,\frac{1}{p d_{AB}^2 \Omega_{AB}} \quad \text{.....(4.29)}$$

where Ω_{AB}, the collision integral, is a function which requires several input values which will not be known for any given scenario that may be present during simulation.

The results in **Table 4.2** show that the diffusivity estimation computed from Chapman-Enskog (Eq. 4.29) method more closely matches the measured self-diffusivity data for methane (Chapman and Cowling 1991). However, Chapman-Enskog is valid only for estimation of binary diffusion (two component) or self-diffusion (single component) coefficients, and is not extensible to an arbitrary number of components. Additionally, Eq. 4.26 of this work predicts the diffusion coefficients of ethane more accurately than the Chapman-Enskog equation (Eq. 4.29).

Other methods exist for estimation of diffusivity for multicomponent mixtures, but these methods require binary interaction parameters for the gases as inputs, which defeats the purpose of a flexible formulation for use in simulation. While our method appears to underestimate diffusivities, it is adequate for our purposes, lacking a more flexible method.

Table 4.2 — Measured results for diffusivity are compared against estimated values from Chapman-Enskog theory, ideal gas assumption, and Eq. 3.26 of this work for the purposes of implicit validation of the Eq. 3.13 for mean free path and diffusivity estimation (Chapman and Cowling 1991).

Gas	T	p	Measured	Chapman-Enskog	Eq. 3.26 of this Work	Ideal Gas
			D			
	K	MPa	10^9 m^2/s			
Methane	303.3	30	62	7.58E+01	4.29E+01	1.44E+02
		40	49	5.68E+01	3.63E+01	1.08E+02
		50	43	4.55E+01	3.26E+01	8.65E+01
	333.1	30	75	9.00E+01	5.11E+01	1.51E+02
		40	60	6.75E+01	4.22E+01	1.13E+02
		50	51	5.40E+01	3.72E+01	9.07E+01
Ethane	303.3	30	18.6	3.46E+01	2.44E+01	4.28E+01
		40	16.7	2.59E+01	2.41E+01	3.21E+01
		50	15.2	2.08E+01	2.32E+01	2.57E+01
	333.1	30	25	4.14E+01	2.88E+01	4.93E+01
		40	21	3.11E+01	2.69E+01	3.69E+01
		50	19.2	2.49E+01	2.57E+01	2.96E+01

4.5 Desorption from Kerogen

In shale gas reservoir systems, more than half of the total gas in place can be stored via surface adsorption. Hydrocarbon gases, as well as carbon dioxide, will physically bond to the surface of the kerogenic media present in the rock, due to the high surface area and high chemical affinity of the hydrocarbon-like kerogen for the hydrocarbon gases.

Desorption of gases from kerogenic media has been extensively studied in coalbed methane reservoir systems. Based on the study of desorption from coalbed methane reservoirs, many models have been proposed to accurately characterize these desorption isotherms, accounting for multicomponent interactions and transient effects. However, the sorptive properties of coal and shale are very different. The Langmuir isotherm (Clarkson and Bustin 1999) for multiple components is believed to be suitably accurate for use in shale gas reservoir systems:

$$V_i = \frac{V_{L,i} B_i p y_i}{1 + \sum_{j=1}^{n} B_j p y_j} \quad \text{.....(4.30)}$$

where V_i is the Langmuir storage density of component i in scf/ton, $V_{L,i}$ is the Langmuir volume constant of component i in scf/ton, B_i is the Langmuir constant of component i in 1/Pa, and y_i is the dimensionless mole fraction. The Langmuir isotherm assumes there is no transient lag between pressure drop and desorption, i.e., instantaneous equilibrium, which is a reasonable assumption due to the very low flow rate within shale. The multicomponent Langmuir model is known to be thermodynamically incorrect when the values of $V_{L,i}$ are significantly different between gas species, which may result in errors.

A consequence of the simultaneous desorption of multiple gas species each having different Langmuir constants and Langmuir volumes is that the species will desorb at different rates. For example, the sorptivity of carbon dioxide is higher than that of any light hydrocarbon, and carbon dioxide will displace hydrocarbon gases from sorption sites. There exists little published data regarding multicomponent Langmuir parameters for shale gas reservoirs. However, a larger body of work concerning coalbed methane reservoirs exists. For the sake of completeness, we use the Billi coal sorptivity parameters listed in **Table 4.3** in our work (Pan and Connel 2008).

Table 4.3 — Desorption parameters for the Billi coalbed methane reservoir correspond to within an acceptable range with those of the Barnett shale. For the initial reservoir pressure used in this study (1500 psi) these values correspond to an initial methane storage of 344 scf/ton, which compares favorably with the Barnett shale range of 300-350 scf/ton (Pan and Connel 2008).

Gas	Langmuir Volume V_L (scf/ton)	Langmuir Parameter B (1/Pa)
CH_4	646.26	9.41E-07
CO_2	983.16	2.11E-06
H_2O	0	0

While the Langmuir storage values in most shale reservoirs will typically be less than the Langmuir storage value in a given coalbed methane reservoir, the relative sorptivity of carbon dioxide versus methane will be similar in both play types.

Table 4.4 — Relative permeability parameters for model. The physical and geochemical interactions of shale with water are complex and no adequate models have been proposed to characterize them. Lacking more accurate tools, we employ Corey's model for relative permeability and van Genuchten's model for capillary pressure are in the numerical model to correctly account for the effect of the presence of water on gas flow.

Corey (1957) Relative Permeability Parameters		
S_{airr}	0.2	(fraction)
S_{girr}	0.02	(fraction)

van Genuchten (1980) Capillary Pressure Parameters		
p_0	2	kPa
S_{airr}	0.2	(fraction)
λ	0.45	
P_{cmax}	5000	kPa
S_{mxA}	1	(fraction)

The vast majority of shale gas and tight gas wells are stimulated via hydraulic fracturing. Typical completion strategies for these reservoirs involve either a vertical well with a vertical bi-wing hydraulic fracture or a horizontal well with multiple transverse hydraulic fractures. The dominant flow regime for the early life of these wells is linear. In order to avoid confounding the effect of interest with complex flow regime effects, we examine only one-dimensional flow.

A Peng-Robinson equation of state is used to model the gas density as a function of pressure (Peng and Robinson 1976). Gas viscosity is modeled by the Chung *et al*. (1988) method. Isothermal conditions are assumed because with a very low flow rate of gas, the effect of Joule-Thompson cooling will be minimal.

Because both gas and water are present, capillary pressure and relative permeability effects must be taken into consideration. We employ the van Genuchten (1980) model of capillary pressure and the Corey (1957) model for relative permeability with the constants found in **Table 4.4**.

For all cases, flow is simulated using the permeability adjustment method of Florence *et al*. (2007) in the model of this work, in this case in the mode of a finite-difference two-phase numerical model. The system is solved via the Jacobian matrix method. Flow is simulated in this model for a period of 100 days, and the concentration and pressure profiles shown below have all evolved after 100 days of flow. A total of 22 simulation cases are studied in **Table 4.5**.

The logic of the design of the cases in **Table 4.5** is to begin by examining the effect of microflow on the simplest possible case – single-phase gas without desorption – and gradually adding transport and storage mechanisms until the presence of water and the presence of desorption are modeled.

Table 4.5 — Microflow parameters used for sensitivity cases. Where 'Microflow Activity' is designated 'No,' base permeability to gas is identical to k_∞, and not enhanced in any way. Where 'Desorption Activity' is designated 'No,' zero desorption effect is indicated; where 'Desorption Activity' is designated 'Yes,' **Table 4.3** sorptivity parameters are employed. In cases 1 through 14 and 19 through 22, Eq. 4.7 is used to estimate r_{pore} from k_∞ and in cases 15 through 18 Eq. 4.7 is employed with ϕ=0.14 rather than 0.05.

Case Number	Permeability to Liquid k_∞ (nd)	Effective Hydraulic Radius r_{pore} (nm)	Presence of Water	Mircoflow Activity	Desorption Activity
1	10	1.25	No	No	No
2	100	3.96	No	No	No
3	10	1.25	No	Yes	No
4	100	3.96	No	Yes	No
5	10	1.25	Yes	No	No
6	100	3.96	Yes	No	No
7	10	1.25	Yes	Yes	No
8	100	3.96	Yes	Yes	No
9	10	1.25	Yes	No	Yes
10	100	3.96	Yes	No	Yes
11	10	1.25	Yes	Yes	Yes
12	100	3.96	Yes	Yes	Yes
13	1000	12.5	Yes	Yes	Yes
14	10000	39.6	Yes	Yes	Yes
15	10	0.748	Yes	Yes	Yes
16	100	2.37	Yes	Yes	Yes
17	1000	7.48	Yes	Yes	Yes
18	10000	23.7	Yes	Yes	Yes
19	10	1.25	Yes	Yes	No
20	100	3.96	Yes	Yes	No
21	1000	12.5	Yes	Yes	No
22	10000	39.6	Yes	Yes	No

We attempt to capture a range of possible scenarios. Cases 1 through 4 use the reservoir parameters contained in **Table 4.6**. The justification for these properties is to provide cases where no water and no

desorption are present, in order to examine the microflow effect in isolation from any effects of relative permeability or sorption-induced compositional shift.

Table 4.6 — Parameters employed in simulation cases 1 through 4.

Parameter		Initial State	
Porosity	ϕ	0.05	Fraction
Initial Methane Concentration in Gas Phase	$y_{G,CH4,i}$	0.9	Mole fraction
Initial Carbon Dioxide Concentration	$y_{CO2,i}$	0.05	Mole fraction
Initial Water Concentration	$y_{H2O,i}$	0.05	Mole fraction
Initial Gas Saturation	$S_{gas,i}$	1.0	Fraction
Temperature	T	300	C
Simulation Time	t	100	days
Initial Reservoir Pressure	p	1500	psi
Constant Fracture Pressure	p_{wf}	100	psi

The next scenario we attempt to capture is analogous to a more realistic tight gas or shale gas case, having a high liquid water content, as well as the potential for significant desorption. In this scenario, describing Cases 5 through 18, properties from **Table 4.7** are used, with **Table 4.4** properties characterizing the relative permeability and capillary pressure effects, and **Table 4.3** containing the sorptive parameters.

Table 4.7 — Parameters employed in cases 5 through 18. Gaseous methane concentration is fixed, while gas phase water and carbon dioxide concentrations is determined by the equation of state.

Parameter		Initial State	
Porosity	ϕ	0.05	Fraction
Initial Methane Concentration in Gas Phase	$y_{G,CH4,i}$	0.75	Mole fraction
Initial Gas Saturation	$S_{gas,i}$	0.5	Fraction
Temperature	T	60	C
Simulation Time	t	100	days
Initial Reservoir Pressure	p	1500	psi
Constant Fracture Pressure	p_{wf}	100	psi

The final scenario is intentionally representative of Barnett Shale reservoir parameters, and is shown in **Table 4.8** and used for Cases 19 through 22. The primary difference between these cases and the true Barnett Shale is that desorption is not accounted for in these cases.

Table 4.8 — Parameters employed in simulation cases 19 through 22. Gas phase methane and ethane concentrations are fixed, while gas phase water and propane concentrations is determined by the equation of state. These values match reported Barnett Shale reservoir parameters.

Parameter		Initial State	
Porosity	ϕ	0.05	Fraction
Initial Methane Concentration in Gas Phase	$y_{G,CH4,i}$	0.95	Mole fraction
Initial Ethane Concentration in Gas Phase	$y_{G,CH4,i}$	0.03	Mole fraction
Temperature	T	95	C
Simulation Time	t	100	days
Initial Reservoir Pressure	p	3000	psi
Constant Fracture Pressure	p_{wf}	1000	psi

Desorption is neglected here because the intent of the study of the microflow effect is to show what degree of compositional shift may be caused solely by fractionation in the nanoporosity. Desorption is already known to be a driver of compositional shift, while the role of microflow is unexplored.

4.6 Results

The goal of performing a numerical sensitivity study is first to demonstrate the identifiable effects of the microflow behavior on rate and composition in porous media, and also to capture the range of potential physically real scenarios which may occur in tight gas and shale gas reservoirs. We begin by specifically examining the effect of microflow where other considerations of transport and storage in porous media such as the presence of water and the presence of sorbed gas are either present or absent.

As a starting point, in **Fig. 4.3** we see the pressure of the gas in the reservoir with respect to distance from the fracture face with various considerations of transport and storage. The obvious consequence of the effective permeability enhancement is that the pressure transient moves further into the reservoir in cases with microflow active.

Additionally, due to the fact that permeability increases even more where pressure has been depleted, the pressure transient forms the characteristic bow shape seen in Case 3, Case 7 and Case 11 of **Fig. 4.3**. This

behavior is expected, and in fact could likely be modeled equally well by the Klinkenberg correction, since the behavior of the pressure transient is not significantly species-dependent.

The sole difference between Cases 1 and 5 in **Fig. 4.3** is that water is present in Case 5 at an initial saturation of 50% while in Case 1 no water is present. This makes almost no difference in the behavior of the pressure transient.

We also observe in **Fig. 4.3** that the general consequence of desorption is to add energy to the system and delay the progression of the pressure transient. This slowing of the pressure transient is a function of the extra energy present in the system due to adsorbed gas, not a consequence of decreased effective permeability.

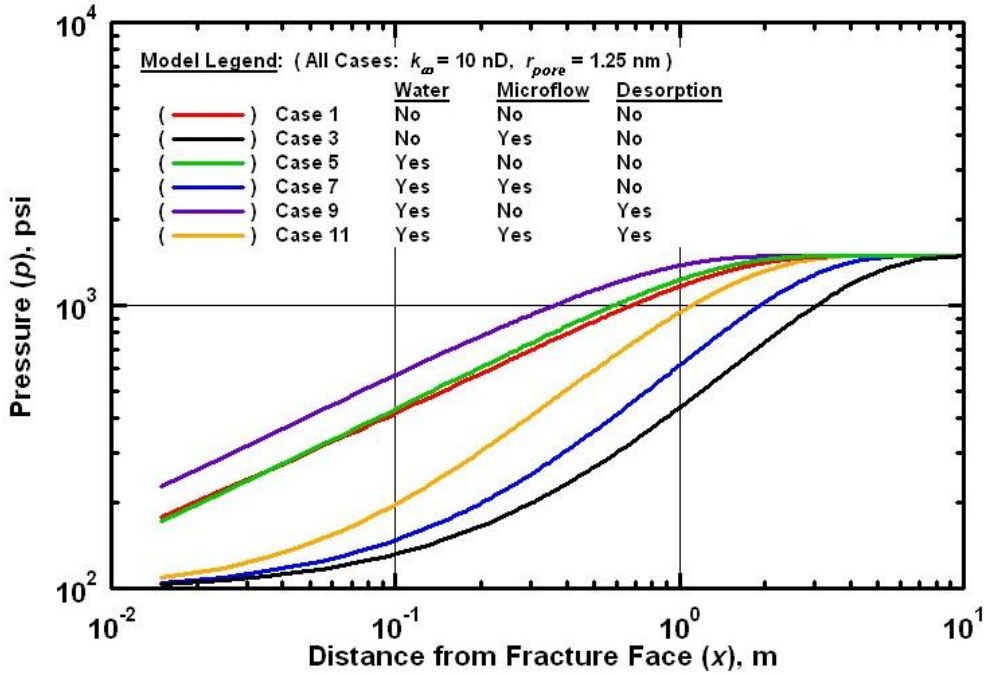

Figure. 4.3 — The gradient of pressure in the reservoir after 100 days varies depending on many parameters, including the presence of water, the presence of desorption, and the assumption of microflow. Case 1 is the simplest possible case, while Case 11 accounts for all the relevant physical phenomena. This case assumes two phases (water and gas) with desorption active. Only odd-numbered cases are shown so that all cases shown will have the same permeability to liquid and the same pore throat radius.

As shown in **Fig. 4.4**, the uneven desorption of the different gases into the pore space results in a significantly different concentration profile. The most striking feature of **Fig. 4.4** is the significantly different methane concentrations at the fracture face for each case, despite the fact that each case possesses identical 75% methane initial gas molar composition. Clearly, the interaction of desorption with microflow is complex.

Examining the difference between Case 7 and Case 11 in **Fig. 4.4** suggests that a model which matches reservoir parameters accounting for desorption but fails to account for microflow-related parameters will yield an incorrect estimate of the contribution of desorption. At the very least, the nonuniqueness of such a match will result in one of the model parameters being significantly wrong. Any assumption of a constant permeability value where microflow is significant is guaranteed to be wrong.

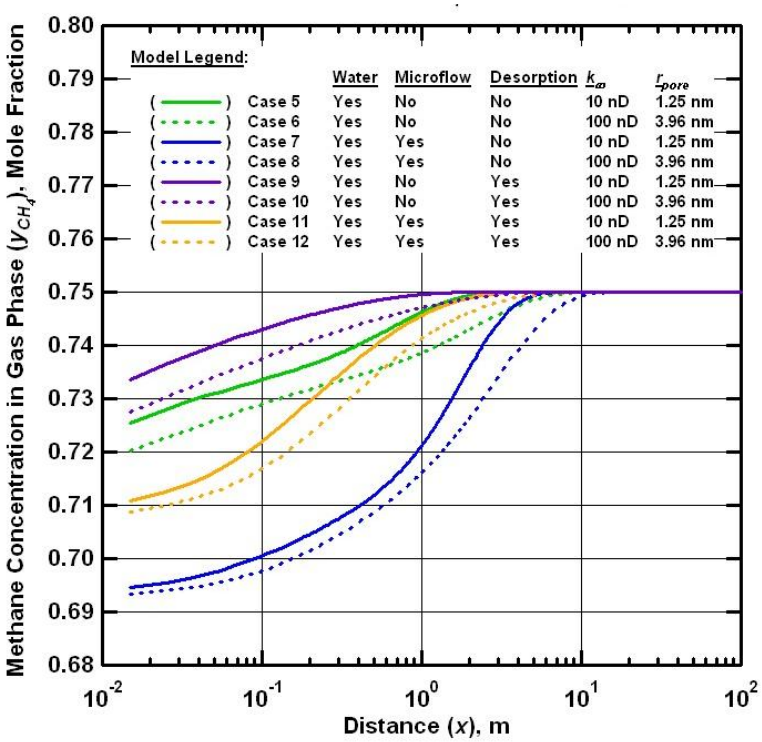

Figure 4.4 — The methane concentration in the gas phase in the reservoir after 100 days varies depending on many factors including desorption, the presence of water, and the assumption of microflow. Desorption appears to reduce the nonlinear steepness of the concentration profile where microflow is present.

The profile of methane concentration in the produced gas over time is a characteristic decline, as shown in **Fig. 4.5**. Where microflow is not considered, the influence of desorption can be seen by comparing Case 5

with Case 9. In either case, the initial gas composition is slightly higher than the initial composition, and diminishes by 2% over the 100 day production period.

Where desorption and microflow are both present (Cases 11 and 12 of **Fig. 4.5**), the concentration of the produced gas changes over the course of 100 days by over 3%. Where microflow is present without desorption, the concentration changes over 5% over 100 days. Where neither desorption nor microflow are present, the change in composition is 2% with most of the change due to evaporation of water.

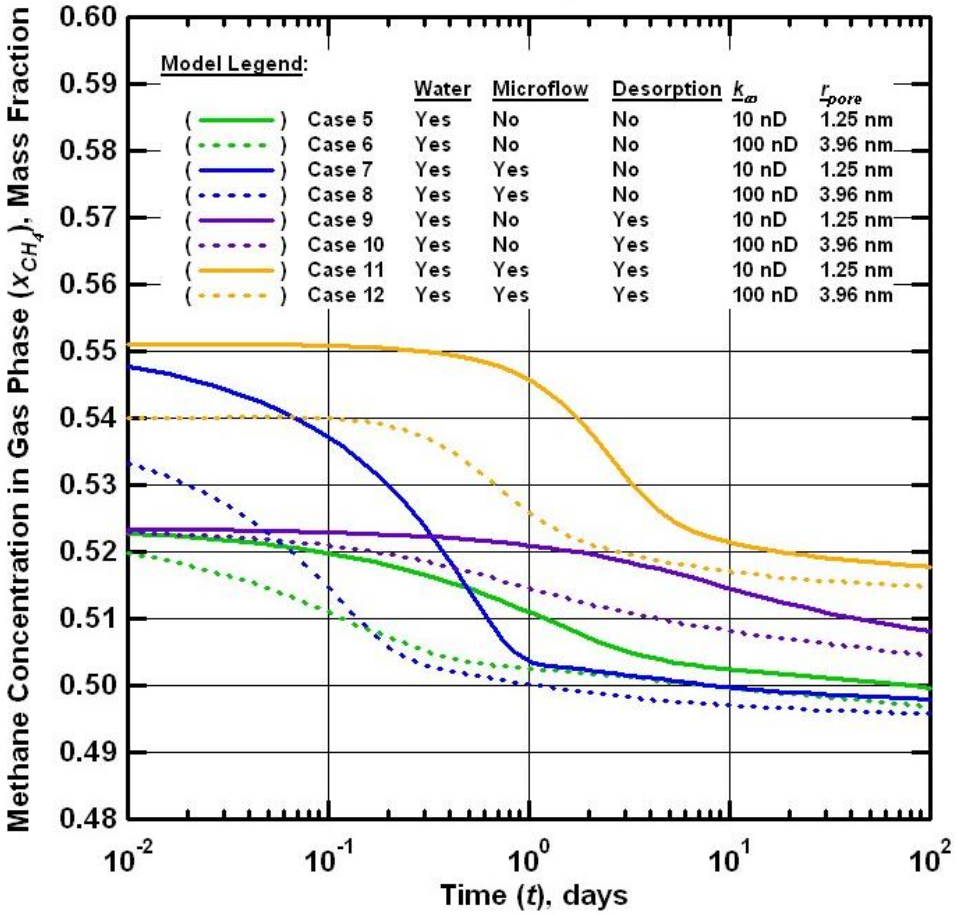

Figure 4.5 — The methane concentration in the produced gas stream varies depending on many factors including desorption, the presence of water, and the assumption of microflow.

An important observation is that in all cases including microflow, the most significant change in concentration occurs within the first ten days; in Case 7 and Case 8 in **Fig. 4.5**, the change occurs within

the first day. In the cases not including microflow and only including desorption, (Cases 9 and 10 in **Fig. 4.5**) the concentration change is much more gradual over time. A signature of microflow thus appears to be a change in concentration of several percent within early production times, coupled with an unexpectedly high initial methane composition.

We see an indication that the remaining gas storage in sorption after 100 days must remain relatively high. Due to the nonlinearity of the desorption isotherm, the majority of the gas stored in sorption will only desorb at lower pressures. Furthermore, the profile of gas desorption in Cases 11 and 12 exhibits the same S-shaped character and increased steepness seen in the pressure profile.

We observe in **Fig. 4.5** that the base case, Case 5, possesses no microflow effect and thus indicates the *in situ* methane concentration in the hydrocarbon component of the gas, adjusted for the change in water composition in the gas phase due to evaporation.

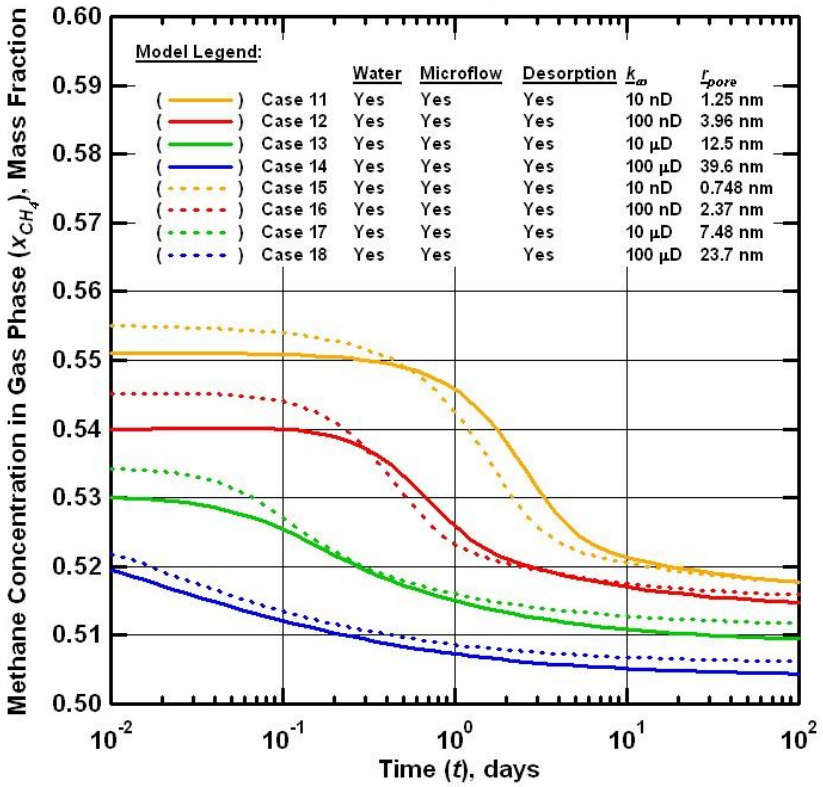

Figure 4.6 — For several cases including all relevant flow physics (water, desorption, and microflow) with various assumptions of r_{pore} given k_∞ the change in methane concentration in the produced gas over time is shown. Higher permeability cases result in lower compositional change.

Fig. 4.6 shows that where all relevant flow physics (water, desorption, and microflow) are present, the produced gas composition will vary significantly with effective pore radius alone. With various assumptions of r_{pore} given k_∞ the change in methane concentration in the produced gas over time is shown to vary by a maximum of 4% in Case 11 over 100 days. Higher permeability results in less compositional shift.

For the lowest permeability case (with the smallest r_{pore}) the initial concentration is 55.5% compared with the initial concentration of the highest permeability case (with the highest r_{pore}) which is 52%, a significant difference. Again, note that all other parameters including pressure and desorption are identical between these cases.Finally, we wish to examine the effect of flow boundaries on the fractionation effect. Flow boundaries may occur in the form of actual reservoir seals such as faults, but are more likely to occur in the form of pseudo-boundaries in tight gas and shale gas reservoirs, where the production envelopes of nearby fractures begin to interfere. The signature of fracture interference in production data is difficult to distinguish from a boundary effect (Mattar *et al*. 2008). In order to study this boundary effect, we employ the reservoir parameters listed in **Table 4.8** which fall within the range of the properties of the Barnett Shale, the most significant shale gas play to date. We show the change in the composition of the produced gas over time in **Fig. 4.7**.

As expected, the lighter, smaller molecules, having larger mean free paths, are more affected by the porous media, and their effective permeability is consequently enhanced more strongly. As a result, the produced gas composition also changes over time, as seen in **Fig. 4.7**. We observe that produced methane composition increases initially and then appears to stabilize after a short period of time, in these cases less than one day. The value at which the composition stabilizes is a function of the degree of the microflow effect. Comparing Case 21 versus Case 19, the produced gas contains 0.05% more methane by mass, which is measurable but not extreme.

As a secondary consequence, the presence of liquid water will cause the gas composition profile to change more significantly with pressure as liquid water vaporizes. Because liquid effective permeability is not enhanced by the microflow effect, the flow of water is far less than the flow of gas, and most depletion of water is due to evaporation into the gas phase followed by convection of the water vapor.

It should also be observed that the concentration of methane in the aqueous phase decreases via exsolution as the pressure drops, though this is largely masked and confounded by the effect of microflow on the produced gas rates. The contribution of exsolution of hydrocarbon gases to total compositional change is extremely minor.

Also we observe that the starting composition of the produced gas will vary significantly from this *in situ* value as a function of the pore throat radius. A characteristic early-time drop in methane concentration occurs in the cases with the most significant microflow effect. This effect lasts no longer than an hour even in the most severe case. However, the steady-state gas composition is still richer in methane than the *in situ* composition would indicate. Case 5 in **Fig. 4.7** indicates the *in situ* methane composition, and clearly the produced gas composition in all other cases is much higher. If a difference in composition can be measured between produced gas composition and composition determined from core analysis, then microflow effects may be the culprit.

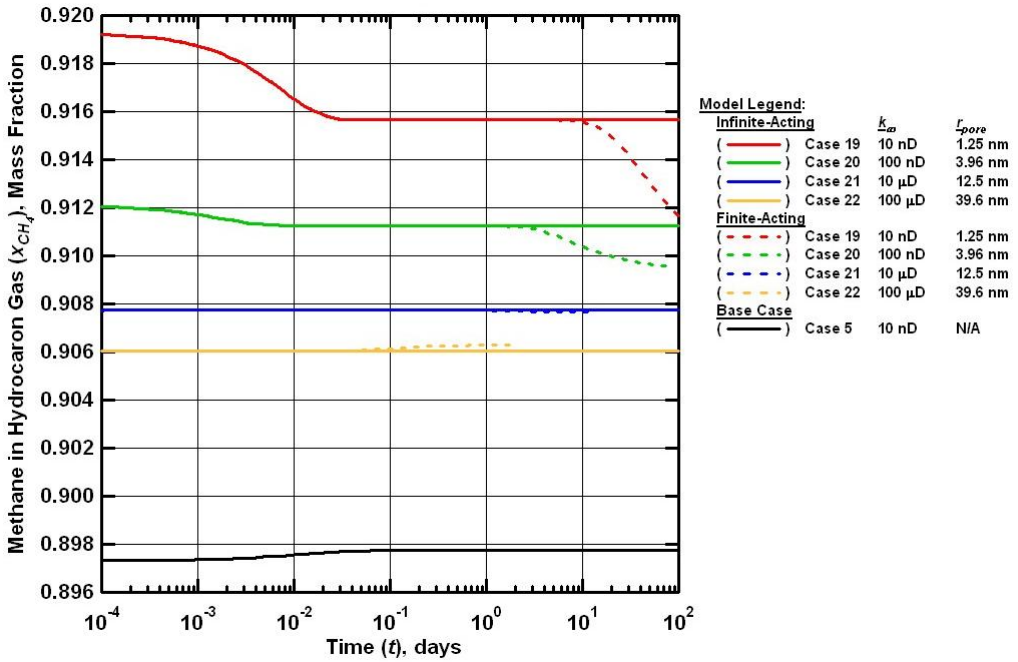

Figure 4.7 — The change in methane composition in the hydrocarbon component of the produced gas phase is shown for cases with similar reservoir properties to the Barnett Shale (listed in **Table 3.8**) with some cases having flow boundaries 1m from the fracture face.

This is where the potential utility of the microflow concept comes into play. If the *in situ* gas composition is known, which is typically the case, and the produced gas concentration deviates from this value by a significant margin, then the effect of microscale flow can potentially be characterized by using the Florence relation in Eq. 4.13 and calculating an effective pore throat radius using Eq. 4.7.

In the cases listed in **Fig. 4.7** as being finite-acting, the flow boundary is placed 1m away from the fracture face. This is a short interval compared to a typical fracturing treatment, but it can be assumed that larger fracture spacing would result in the same production signature, except delayed in time.

When the flow boundary is felt by the pressure transient, the concentration of methane in the hydrocarbon gas component drops severely. Analogously, we can say that the relative composition of ethane and propane in the produced gas increase when this reservoir boundary is felt. This effect is the observed "richening" of the produced gas in tight gas and shale gas wells. Where the reservoir is highly fractured, either due to induced or natural fracturing, the behavior of a given block of matrix may be conceptually approximated as an internal flow boundary, and the same effect would likely be observed.

4.7 Conclusions

The fractionating effect of nanoscale pores on mixed gases has been studied in context of zeolite separation media and has been observed empirically in tight gas reservoirs. This work examines existent methods by which to characterize this phenomenon, and proposes a means by which to model and predict its effects.

Implementation of the microflow permeability adjustment model into a robust fluid flow modeling tool demonstrates the capability to predict the change of produced gas composition with time in ultratight reservoirs and potential utility in sampling changes in gas composition with time in these reservoirs in order to better characterize the rock properties. This work also attempts to reconcile the mystery of unexpectedly high rates of gas produced from shale gas and tight gas plays.

Where canister desorption data from shale gas reservoirs is available, it should possible to determine Langmuir parameters for desorption. Performing core analysis using the Florence *et al.* (2007) method (similarly to how the Klinkenberg (1941) method is commonly used) will provide characterization of the microflow effect. If both desorption and microflow are correctly measured, modeling of flow and composition change becomes possible. Furthermore, there is a potentially for core analyses involving flow-through of gases of known composition with the composition of the effluent gas measured to determine the microflow properties of the rock.

The identification of boundary dominated flow in these reservoir types becomes verifiable through measurement of a sharp compositional shift ("richening") where boundaries or fracture interference effects come into play.

CHAPTER V

SUMMARY AND CONCLUSIONS

The purpose of this work is to provide a superior understanding of tight gas and shale gas reservoir systems using a precise forward-modeling study of possible physical configurations of these systems. The approach to achieve this goal has been to build a numerical model capable of capturing all geometric and petrophysical aspects of these reservoirs, and to study the effects of varying the model parameters on flow behavior.

Chapter I illustrates the basic design of the model and the validation process of the tool. This validation included a comparison against an analytical solution, a commercial package (Eclipse 2008) and a Haynesville shale gas well with model match parameters from (Ecrin 2009). The model performed well in all cases. The model has advanced to the point that no other technologies exist against which it can be verified. Thus, we ensure that the basic functionality is correct by checking against commercial and analytical schemes, and then proceed from that point. We note that the model match of the Haynesville shale gas well should not necessarily be interpreted as an indicator that the model contains all relevant flow physics; on the contrary, it is possible to match early time data from shale gas reservoirs with a variety of incorrect or inapplicable models. An accurate model match does not imply a correct physical representation.

Chapter II describes the current literature pertaining to tight gas and shale gas geology and petrology and details the models appropriate for use in studying all facets of these reservoir systems. A literature search of this nature is never truly complete, because new insights reveal unexpected opportunities for application of existing models, and new models are continually being proposed. The models described in this section include closed-form relations for Forchheimer (1901) flow parameter estimation for single and two-phase flow, various types of pressure-dependent porosity and permeability relations to approximate the effects of pore compressibility, the Klinkenberg (1941) and Florence *et al.* (2007) models for permeability correction due to microscale flow effects, wettability and relative permeability effects in the Corey (1957) and van Genuchten (1980) models, and a simple but acceptable Langmuir (1916) model for gas desorption (Li and Engler 2001; Kutasov 1993; Frederick and Graves 1994). These models are all programmed into the reservoir simulator.

Chapter III showcases a forward-modeling sensitivity study of the effects of various reservoir parameters on tight gas and shale gas reservoir systems. The features varied in this study included adsorbed gas, fracture conductivity, fracture spacing, matrix permeability, and various altered configurations of the fracture system. The study showed that the effect of desorption can be normalized by a time-scaling factor, indicating possible diagnostic utility. If fracture configurations can be assessed through joint

production data analysis and microseismic interpretation, then the time to fracture interference can be estimated. If the measured time to fracture interference deviates from the predicted time, the culprit may be the time-scaling effect of desorption. Another important conclusion of the forward-modeling study was that the extent and distribution of the secondary fracture network strongly controls early time rate. Even a system of low conductivity fractures will tend to significantly enhance rate compared with a single planar fracture through solid tight sandstone or shale.

While Chapter III examines transient macro-scale flow effects, Chapter IV focuses on micro-scale flow in the nanoporosity of the shale kerogen and the authigenic clay of the tight gas reservoirs. In Chapter III, a multi-component formulation of the mean free path (Eq. 3.13) is suggested, as well as a new method for estimation of diffusivity factors in multicomponent gas mixtures (Eq. 3.26). These equations are shown to be accurate to within a similar order as widely accepted equations such as the Chapman-Enskog equation (Chapman and Cowling 1991). Through the implementation of this model we show that compositional shift of produced gas in tight gas and shale gas reservoirs is a real possibility even at moderately high pressures. We show that this compositional shift will appear as a constant altered composition in transient flow and a constantly changing composition in boundary-dominated flow.

This study has provided several novel observations and conclusions which may be used for advancing the technology of production data analysis and interpretation in tight gas and shale gas reservoir systems.

NOMENCLATURE

Variables:

a = Empirical constant of Cooke (1973) model (dimensionless)

b = Empirical constant of Cooke (1973) model (dimensionless)

B = Formation volume factor, bbl/stb

B_i = Multicomponent Langmuir parameter, 1/Pa

b_K = Klinkenberg constant (Pa)

c = Constant of Klinkenberg approximation, approximately 1 (dimensionless)

c_1 = Constant of rarefaction equation, 4.0 (dimensionless)

c_2 = Constant of rarefaction equation, 0.4 (dimensionless)

c_f = Formation compressibility, 1/psi

C_{fD} = Dimensionless fracture conductivity (dimensionless)

c_p = Pore compressibility, 1/psi

c_t = Total compressibility, 1/psi

d_f = Fracture spacing, ft

$D_{G,i}$ = Diffusion coefficient of species i in the gas phase, m^2/s

d_k = molecular kinetic diameter, m

E_1 = Error function (operator)

h = Reservoir thickness, ft

J = Diffusive molar flux, mol/m^2

k = Matrix permeability, md

k_0 = Initial matrix permeability, md

k_a = Apparent permeability to gas phase, md

k_B = Boltzmann's constant,$1.3806503 \times 10^{-23}$ m^2-kg/(s^2-K)

k_f = Fracture permeability, md

k_g = Permeability to gas phase, md

k_m = Matrix permeability, md

Kn = Knudsen number (dimensionless)

k_{rw} = Relative permeability to aqueous phase (dimensionless)

k_w = Intrinsic permeability to aqueous phase, md

k_∞ = Intrinsic permeability or permeability at infinite pressure, md

l_{char} = Characteristic feature length (pore or capillary radius), cm

L_w = Horizontal well length, ft

M = Molecular mass, g/mol

N_A = Avogadro's number, 6.02×10^{23} molecules

n_v = Moles of gas per unit volume, mol/m^3

p = Pressure, psi

P_{cmax} = Maximum capillary pressure of van Genuchten, kPa

p_D = Dimensionless pressure (dimensionless)

p_0 = Pressure parameter of van Genuchten, kPa

p_i = Initial reservoir pressure, psi

p_r = Pressure at point r in reservoir, psi

p_{wf} = Wellbore flowing pressure, psi

p_L = Langmuir pressure, psi

q = Rate, bbl/day or mscf/day

q_{Dd} = Dimensionless rate derivative (dimensionless)

q_{Ddi} = Dimensionless rate integral (dimensionless)

q_{Ddid} = Dimensionless rate integral derivative (dimensionless)

r = Radius, ft

r_D = Dimensionless radius (dimensionless)

r_{pore} = Pore throat radius (cm)

r_w = Wellbore radius, ft

R = Ideal gas constant, 8.314 J/K-mol

S_w = Water phase saturation, fraction

S_G = Gas phase saturation, fraction

S_{airr} = Irreducible aqueous saturation of Corey *et al.*[8], fraction

S_{girr} = Gas phase saturation, fraction

S_{wi} = Initial water saturation, fraction

t = Time, days or seconds

T = Temperature, K

t_D = Dimensionless time (dimensionless)

t_{Dd} = Dimensionless time derivative (dimensionless)

v = Flow velocity, m/s

$\bar{v}$ = Average velocity, m/s

$\overline{v_{rel}}$ = Relative molecular velocity, m/s

$\vec{v}$ = Molecular velocity vector, m/s

$\vec{v}_{rel}$ = Relative molecular velocity vector, m/s

V_L = Langmuir volume, scf/ton

w = Fracture width, ft

x = Distance from production source, m

x_f = Fracture half-length, ft

$X_{G,i}$ = Mass fraction of species i in the gas phase, fraction

y = Mole fraction, fraction

Greek Symbols:

α = Rarefaction parameter[34] (dimensionless)

α_0 = Constant of rarefaction equation[34], 64/15π (dimensionless)

β = Forchheimer nonlinear flow parameter, 1/ft, 1/cm or 1/m

ϕ = Porosity, fraction

τ = Variable of integration (dimensionless)

τ_G = Tortuosity (dimensionless)

ϕ_0 = Initial porosity, fraction

ρ = Density, kg/m^3

ρ_G = Gas phase density, kg/m^3

δ = Constrictivity (dimensionless)

$\bar{\lambda}$ = Mean free path, m

λ = Parameter of van Genuchten[7] (dimensionless)

μ = Viscosity, cP

θ = Langmuir storage, scf/ton

Ω_{AB} = Collision integral of Chapman-Enskog (dimensionless)

Subscripts:

i = Index of the *i*-th component.

j = Index of the *i*-th component.

a = Component of interest in a binary mixture

b = Second component in a binary mixture

G = Gas phase

CH4 = Methane component.

CO2 = Carbon dioxide component.

H2O = Water component.

REFERENCES

Bird, R.B., Stewart, W.E., and Lightfoot, E.N. 2007. *Transport Phenomena*. New York: John Wiley & Sons, Inc.

Chapman, S., Cowling, T.G. 1991. *The Mathematical Theory of Non-uniform Gases*. Cambridge, UK: Cambridge University Press.

Chapman, Stephen J. 2008. *Fortran 95/2003 for Scientists and Engineers*. Boston. McGraw-Hill.

Chen, N.Y., Degnan, T.F., Smith, C.M. 1994. *Molecular Transport and Reaction in Zeolites*. John Wiley & Sons, Inc.

Chung, T.H., Ajlan, M., Lee, L.L., and Starling, K.E. 1988. Generalized Multiparameter Correlation for Nonpolar and Polar Fluid Transport-Properties. *Industrial & Engineering Chemistry Research* **27** (4): 671-679. DOI: 10.1021/ie00076a024.

Cinco-Ley, H. Samaniego-V., F., and Domingues, A. 1978. Transient Pressure Behavior for a Well with a Finite-Conductivity Vertical Fracture, *SPE J*. **57** (3-4): 253-264.

Civan, F. 2008. Effective Correlation of Apparent Gas Permeability in Tight Porous Media. *Transp. Porous Med*. **82** (2) 375-384. DOI:10.1007/s11242-009-9432-z.

Clarkson, C.R.. and Bustin, R.M. 2000. Binary gas adsorption/desorption isotherms: effect of moisture and coal composition upon carbon dioxide selectivity over methane. *International Journal of Coal Geology*. **42** (4): 241-271. DOI: 10.1016/S0166(99)00032-4.

Collins, John P. 1996. Catalytic Dehydrogenation of Propane in Hydrogen Permselective Membrane Reactors. *Ind. Eng. Chem. Res*. **35** (12): 4398-4405. DOI: 10.1021/ie960133m.

Cooke, C.E., Jr. 1973. Conductivity of Fracture Proppants in Multiple Layers. *JPT*. **25** (9): 1101-1107. SPE-4117-PA. DOI: 10.2118/4117-PA.

Corey, A.T. 1957. Measurement of water and air permeability in unsaturated soil. *Soil Sci. Soc. Am. Proc.* **21**:7-10.

Currie, S.M., Ilk, D., Blasingame, T.A. 2010. Continuous Estimation of Ultimate Recovery. SPE paper 132352 presented at the Unconventional Gas Conference, Pittsburgh, Pennsylvania, 23-25 February.

Davies, J.P., Davies, D.K. 2001. Stress-Dependent Permeability: Characterization and Modeling. *SPE J*. **6** (2): 224-235. SPE-71750-PA. DOI: 10.2118/71750-PA.

Eclipse Reservoir Engineering Software. 2009. Schlumberger, http://slb.com/.

Florence, F.A., Rushing, J.A., Newsham, K.E., and Blasingame, T.A. 2007. Improved Permeability Prediction Relations for Low-Permeability Sands. SPE paper 107954 presented at the SPE Rocky Mountain Oil & Gas Technology Symposium held in Denver, Colorado, 16-18 April.

Forchheimer, P. 1901. Wasserbewewegung durch Boden. *ZVDI* **45**, 1781.

Frederick Jr., D.C. and Graves, R.M. 1994. New Correlations To Prediction Non-Darcy Flow Coefficients at Immobile and Mobile Water Saturation. Paper SPE 28451 presented at the 1994 SPE Annual Technical Conference and Exhibition, New Orleans, Sept. 25-28.

Gao, C., Lee, J.W., Spivey, J.P., and Semmelbeck, M.E. 1994. Modeling Multilayer Gas Reservoirs Including Sorption Effects. SPE paper 29173 presented at the SPE Eastern Regional Conference & Exhibition, Charleston, West Virginia, 8-10 November.

Gupta, V. 1995. Evidence for single file diffusion of ethane in the molecular sieve AIPO4-5. *Chemical Physical Letters*. **247**, 596-600.

Hill, D.G., and Nelson, C.R. 2000. Gas Productive Fractured Shales: An Overview and Update. *Gas TIPS* **6** (3): 4-13.

Ilk, D., Hosseinpour-Zonoozi, N., Amini, S., Blasingame, T.A. 2007. Application of the β-Integral Derivative Function to Production Analysis. SPE paper 107967 presented at the SPE Rocky Mountain Oil & Gas Technology Symposium held in Denver, Colorado, 16-18 April.

Ivanova, E. 2007. Ethanol Vapours Adsorption by Natural Clynoptilolite. *Journal of the University of Chemical Technology and Metallurgy*. **42**, 391-398.

Karniadakis, G.E., and Beskok, A. 2001. *Microflows: Fundamentals and Simulation*. New York: Springer.

Klinkenberg, L.J. 1941. The Permeability of Porous Media to Liquid and Gases. Paper presented at the API 11th Mid Year Meeting, Tulsa, Oklahoma (May 1941); in *API Drilling and Production Practice* (1941), 200-213

Kutasov, I.M. 1993. Equation Predicts Non-Darcy Flow Coefficient. *Oil & Gas Journal* (March 15, 1993) 66-67.

Langmuir, I. 1916. The constitution of fundamental properties of solids and liquids. *J. Am. Chem. Soc*. **38**, 2221-95

Li, D., Engler, T.W. 2001. Literature Review on Correlations of the Non-Darcy Coefficient. SPE paper 70015 presented at the SPE Permian Basin Oil and Gas Recovery Conference held in Midland, Texas, 15-16 May.

Mattar, L., Gault, B., Morad, K., Clarkson, C.R., Freeman, C.M., Ilk, D., and Blasingame, T.A. 2008. Production Analysis and Forecasting of Shale Gas Reservoirs: Case History-Based Approach. SPE paper 119897 presented at the SPE Shale Gas Production Conference held in Fort Worth, Texas, 16-18 November.

McKee, C.R., Bumb, A.C., Koenig, R.A. 1988. Stress-Dependent Permeability and Porosity of Coal and Other Geologic Formations. *SPE Form Eval* **3** (1): 81-91. SPE-12858-PA. DOI: 10.2118/12858-PA.

Medeiros, F., Ozkan, E., and Kazemi, H. 2006. A Semianalytical, Pressure-Transient Model for Horizontal and Multilateral Wells in Composite, Layered, and Compartmentalized Reservoirs. SPE paper 102834 presented at the SPE Annual Technical Conference and Exhibition held in San Antonio, Texas, 24-27 September.

Medeiros, F., Ozkan, E., and Kazemi, H. 2007. Productivity and Drainage Area of Fractured Horizontal Wells in Tight Gas Reservoirs. SPE paper 108110 presented at the Rocky Mountain Oil & Gas Technology Symposium held in Denver, Colorado, 16-18 April.

Millington, R.J., and Quirk, J.P, 1961. Permeability of porous solids. *Trans. Faraday Soc*. **57**:1200-1207.

Pan, Z., Connell, L.D. 2008. Comparison of adsorption models in reservoir simulation of enhanced coalbed methane recovery and CO2 sequestration in coal, *Int. J. Greenhouse Gas Control*. **3** (1): 77-89. DOI:10.1016/j.ijggc.2008.05.004.

Peng, DY, and Robinson, DB (1976). A New Two-Constant Equation of State.. *Industrial and Engineering Chemistry: Fundamentals* **15**: 59–64. doi:10.1021/i160057a011

Raghavan, R.S., Chen, C., and Agarwal, B. 1997. An Analysis of Horizontal Wells Intercepted by Multiple Fractures. SPE paper 27652 presented at the SPE Permian Basin Oil and Gas Recovery Conference held in Midland, Texas, 16-18 March.

Reyes, L., Osisanya, S.O. 2002. Empirical Correlation of Effective Stress Dependent Shale Rock Properties. *JCPT.* **41** (12): 47-53.

Sadakane, M. 2008. Molybdenum-Vanadium-Based Molecular Sieves with Microchannels of Seven-Membered Rings of Corner-Sharing Metal Oxide Octahedra. *Angewandte Chemie*. **120** (13): 2527-2530. DOI: 10.1002/ange.200705448.

Sampath, K., Keighin, C.W. 1982. Factors Affecting Gas Slippage in Tight Sandstones of Cretaceous Age in the Uinta Basin. *JPT*. **34** (11): 2715-2720.

Schettler, P.D., and Parmely, C.R. 1991. Contributions to Total Storage Capacity in Devonian Shales. SPE paper 23422 presented at the SPE Eastern Regional Meeting held in Lexington, Kentucky, 22-25 October.

TOUGH+ Numerical Simulator. 2008. Lawrence Berkeley National Laboratory, http://esd.lbl.gov/tough+/.

Ecrin Computer Software. Kappa. 2009. http://www.kappaeng.com/.

van Genuchten, M.T.A. 1980. A closed-form equation for predicting the hydraulic conductivity of unsaturated soils. *Soil Sci. Soc. Am. J*. **44**: 892-898.

van Kruysdijk, C.P.J.W. and Dullaert, G.M. 1989. A Boundary Element Solution of the Transient Pressure Response of Multiple Fractured Horizontal Wells. Paper presented at the 2nd European Conference on the Mathematics of Oil Recovery, Cambridge, England.

Ward, J.S., Morrow, N.R. 1987. Capillary Pressures and Gas Relative Permeabilities of Low-Permeability Sandstone. SPE paper 13882 presented at the SPE Low Permeability Gas Reservoirs Symposium held in Denver, Colorado, 19-22 May.

VITA

Name:	Craig Matthew Freeman
E-mail Address:	tamuic@gmail.com
Education:	Texas A&M University, College Station, Texas, USA M.S., Petroleum Engineering May 2010
	Texas A&M University, College Station, Texas, USA B.S., Chemical Engineering August 2007
Affiliations:	Society of Petroleum Engineers